

# Metallic Magnetic Calorimeters for Particle Detection

C. Enss,<sup>1</sup> A. Fleischmann,<sup>1</sup> K. Horst,<sup>1</sup> J. Schönefeld,<sup>1</sup> J. Sollner,<sup>1</sup>  
J. S. Adams,<sup>2</sup> Y. H. Huang,<sup>2</sup> Y. H. Kim,<sup>2</sup> and G. M. Seidel<sup>2,\*</sup>

<sup>1</sup>Kirchhoff-Institut für Physik, Universität Heidelberg, D-69120 Heidelberg, Germany

<sup>2</sup>Physics Department, Brown University, Providence, Rhode Islands 02912, USA

(Received July 7, 2000; revised September 5, 2000)

*The principles and theory of operation of a magnetic calorimeter, made of a dilute concentration of paramagnetic ions in a metallic host, is discussed in relation to the use of such a device as a detector of x-rays. The response of a calorimeter to the absorption of energy depends upon size, heat capacity, temperature, magnetic field, concentration of spins and interactions among them. The conditions that optimize the performance of a calorimeter are derived. Noise sources, especially that due to thermodynamic fluctuations of the electrons in the metal, are analyzed. Measurements have been made on detectors in which Er serves as the paramagnetic ion and Au as the host metal. The measured resolution of a detector with a heat capacity of  $10^{-12}$  J/K was 12 eV at 6 keV. In a detector suitable for use with hard x-rays up to 200 keV a resolution of 120 eV was obtained. Calculations indicate that the performance of both detectors can be improved by an order of magnitude. At temperatures below 50 mK, the time response of the Au:Er calorimeters to an energy deposition indicates the presence of an additional heat capacity, which we interpret as arising from the quadruple splitting of the Au nuclei in the electric field gradients introduced by the presence of the Er ions.*

## 1. INTRODUCTION

In recent years important advances have been made in astro/particle physics that have deepened our understanding of the nature of the universe and the fundamental properties of matter. Much of this experimental progress has been made possible by technological developments in others fields—optics, computers, semiconductors, etc. In this vein, the emerging technology of cryogenic particle detection is now poised to make major

\*E-mail: seidel@holley.physics.brown.edu

contributions to a variety of experiments in astrophysics. Cryogenic particle detectors are being developed to make possible experiments, which otherwise could not be performed, in such areas as x-ray astronomy, dark matter detection and solar neutrino detection. Among the more promising technologies are thermistors, superconducting transition-edge sensors, and superconducting tunnel junctions. This research involves the study of magnetic microcalorimeters for particle detection.

With the development of low noise SQUIDS it is possible to measure extremely small changes in the magnetization of materials at low temperatures. Double junction dc SQUIDS are specifically designed to sense variations in the magnetic flux threading the superconducting loop connecting the junctions. With such a device Ketchen *et al.*<sup>1</sup> demonstrated the ability to observe with a 1 second time constant the change in magnetization associated with the reorientation of 3000 electron spins, which in a field of 5 mT corresponds to a change in energy of  $4 \times 10^{-3}$  eV. They also pointed out that improvements in technology should make possible substantial increases in sensitivity beyond what they already have achieved.

We have initiated a research program<sup>2</sup> to measure with high precision the absorption of energy of a single quantum of electromagnetic radiation in a microcalorimeter by sensing an associated change in magnetization of the calorimeter. To obtain a large magnetic response the thermodynamic system should have a large temperature-dependent magnetization,  $\partial M/\partial T$ , and a small heat capacity,  $C$ . The change in magnetic moment  $\delta m$  of a sample of volume  $V$  upon the absorption of energy  $\delta \varepsilon$  is

$$\delta m = V \frac{\partial M}{\partial T} \frac{\delta \varepsilon}{C}. \quad (1)$$

This research on magnetic calorimetry is motivated by the desire to develop a high-resolution energy-dispersive detector with high quantum efficiency in the soft and hard x-ray regions of the electromagnetic spectrum. There are several reasons for believing that a SQUID-based magnetometer might provide a superior means of measuring energy absorption in a calorimeter at low temperatures. Many materials possess large temperature dependent magnetizations. The most sensitive thermometers in use today,<sup>3</sup> with a resolution of better than 1 part in  $10^{10}$ , are based on the measurement of magnetization using SQUIDS.

In the course of this research we have investigated experimentally and theoretically the performance of magnetic calorimeters. Section 2 contains a theoretical discussion of the important properties of magnetic calorimeters including material parameters, sensitivity, noise and relaxation times. Details of the experimental apparatus and data analysis are presented in Section 3.

In Section 4, the results of the measurements are related to our theoretical understanding of properties of materials and magnetic calorimeters. Section 5 contains a brief discussion of some of the potential advantages that magnetic calorimeters bring to particle detection.

## 2. PRINCIPLES

The characteristics of magnetic calorimeters differ in two important respects from those of other technologies for cryogenic particle detection. Firstly, a magnetic calorimeter is a well characterized thermodynamic system consisting of an absorber, in which the energy of the particle is converted to heat, and a sensor, which measures that energy. If the thermodynamic properties of the sensor and absorber are known, then the response of the calorimeter upon the absorption of energy can be calculated accurately. Secondly, the measured signal, proportional to the change in flux in a SQUID circuit, depends in a well defined manner upon the size of the magnetic sensor and the geometry of both the pick up loop and the sensor. In optimizing the performance of a calorimeter/detector, the size of the magnetic sensor and the concentration of magnetic ions become variables whose optimal values depend upon the application for which the device is designed.

Umlauf and co-workers<sup>4</sup> were the first to investigate the use of low-temperature magnetic calorimetry for particle detection. They concentrated their research on detectors in which the sensor was a system of paramagnetic ions in a dielectric host. In terms of sensitivity to energy, there is perhaps no material that can match cerium magnesium nitrate (CMN) in the temperature range down to a few millikelvin. Because of the particular crystal structure of CMN and the anisotropic  $g$ -factor of the cerium ion in this crystal, the dipolar interactions are extremely weak even in the concentrated paramagnetic salt. Magnetic ordering sets in only at very low temperatures; contributions to the heat capacity from spin-spin interactions are very small. However, the problem for particle detection with the use of dielectric hosts is, quite generally, the very slow response of the magnetic system to energy changes. The spin-phonon coupling is weak so that time constants of minutes or longer are not unusual at low temperatures. To circumvent this difficulty we have chosen to work with a dilute concentration of paramagnetic ions embedded in a metal where the localized paramagnetic spins are strongly coupled to the conduction electrons. Time constants for establishing thermal equilibrium can be well below a microsecond. The penalty one pays in working with metallic hosts is related with the enhanced exchange interactions among the paramagnetic ions.

## 2.1. Materials

If the only term in the Hamiltonian of a system of paramagnetic ions with spin  $\mathbf{S}$  were the Zeeman interaction with an applied magnetic field  $\mathbf{B}$ , expressed as  $H = g\mu_B \mathbf{S} \cdot \mathbf{B}$ , then Eq. (1) is, very simply,

$$\delta m = -\frac{\delta \varepsilon}{B} \quad (2)$$

However, any real system is far more complex than this. We must include the heat capacity of the host material in which the paramagnetic ions are located and the heat capacity of the material used to stop the x-rays. Also, in a metal the indirect exchange interaction between localized spins, the Ruderman–Kittel–Kasuya–Yosida (RKKY) interaction, has a major influence on the performance of the calorimeter. The heat capacity of the conduction electrons is, under the conditions we shall be investigating, small compared to that of the spin system.

The choice of host metal and of paramagnetic ion is influenced by technical issues such as ease of fabrication, stability etc., but is also determined by the need for having a small RKKY exchange interaction. Ions in the 4f series are better in this regard than are those in the 3d and 4d transition series because of their weaker interactions with the conduction electrons. And among the rare earths those with a small projection of the intrinsic spin of the ion onto the effective spin of the crystal field ground state (deGennes factor<sup>5</sup>) are preferable for the same reason. The  $\text{Er}^{3+}$  ion appears to be one of the better candidates in this regard. This research is based on the use of gold as the metallic host, since it has many technical virtues and the properties of Er in this metal are well known. A semimetal may possibly be a better choice of host—the RKKY interaction is smaller in such materials because of the dependence of the interaction on the density of electronic states at the Fermi level—but far less is known about Er in such systems.

The RKKY interaction between a pair of localized 4f ions  $i$  and  $j$  separated by a distance  $r_{ij}$  is given by<sup>6,7</sup>

$$H_{\text{RKKY}} = -9\pi \frac{Z^2 J_{\text{sf}}^2}{\varepsilon_F} \left[ \left( \frac{g}{g_\Lambda} \right)^2 (g_\Lambda - 1)^2 \right] \frac{F(2k_F r_{ij})}{(2k_F r_{ij})^3} \mathbf{S}_i \cdot \mathbf{S}_j, \quad (3)$$

where  $J_{\text{sf}}$  is the coupling energy between the conduction electrons and the localized 4f electrons of the magnetic ion,  $g_\Lambda$  is the Lande  $g$ -factor of the free ion,  $k_F$  and  $\varepsilon_F$  are the Fermi wave vector and energy respectively,  $Z$  is the number of conduction electrons per atom, and the function  $F$  is given by

$$F(x) = \cos(x) - \sin(x)/x. \quad (4)$$

In Eq. (3) the RKKY interaction is expressed in terms of the effective spin  $\mathbf{S}$  of the ground state Kramer's doublet. The quantity in brackets  $[(g/g_\Lambda)^2 \times (g_\Lambda - 1)^2]$ , which does not appear in many formulations of the RKKY exchange,<sup>6</sup> accounts for the projection of the intrinsic spin of the ion onto the effective spin of the ground state.

We find it convenient to write the interaction in the form<sup>8</sup>

$$H_{\text{RKKY}} = \alpha \frac{\mu_0}{4\pi} \frac{(g\mu_B)^2}{r_{ij}^3} F(2k_F r_{ij}) \mathbf{S}_i \cdot \mathbf{S}_j, \quad (5)$$

where

$$\alpha = -\frac{36\pi^2 Z^2 J_{\text{sf}}^2}{\mu_0 (2k_F)^3 \varepsilon_F \mu_B^2} \left[ \frac{g_\Lambda - 1}{g_\Lambda} \right]^2, \quad (6)$$

so that the magnitude of the RKKY interaction can be readily compared to that of the dipolar interaction.

## 2.2. Sensitivity

In order to calculate the influence of spin-spin interactions on the performance of a magnetic calorimeter we have determined numerically the probability distribution of interaction energies for paramagnetic ions with  $S=1/2$  randomly distributed on an Au lattice. The calculations have been carried out for a number of different concentrations with the strength of the interaction,  $\alpha$ , an adjustable parameter. The RKKY interaction is treated in the mean field approximation, i.e., taken to be of the form  $S_{z_i} S_{z_j}$ . This is a reasonable approximation for analyzing calorimetric data at temperatures well above the spin glass transition. It cannot provide a thermodynamic description of the system where significant ordering occurs.

A plot of the probability distribution of exchange fields for a concentration of 300 ppm is illustrated in Fig. 1 in the absence of an applied magnetic field. Because the distribution is dependent on the relative occupation of the  $S_z = \pm 1/2$  states of the interacting ions, it varies with applied field and temperature. The discrete nature of the host lattice is clearly evident in the plot of the distribution in Fig. 1. However, the overall shape of the energy distribution is fit well by the relation

$$P(h) = \frac{4\delta h}{\pi} \frac{h^2}{(h^2 + (\delta h)^2)^2}, \quad (7)$$

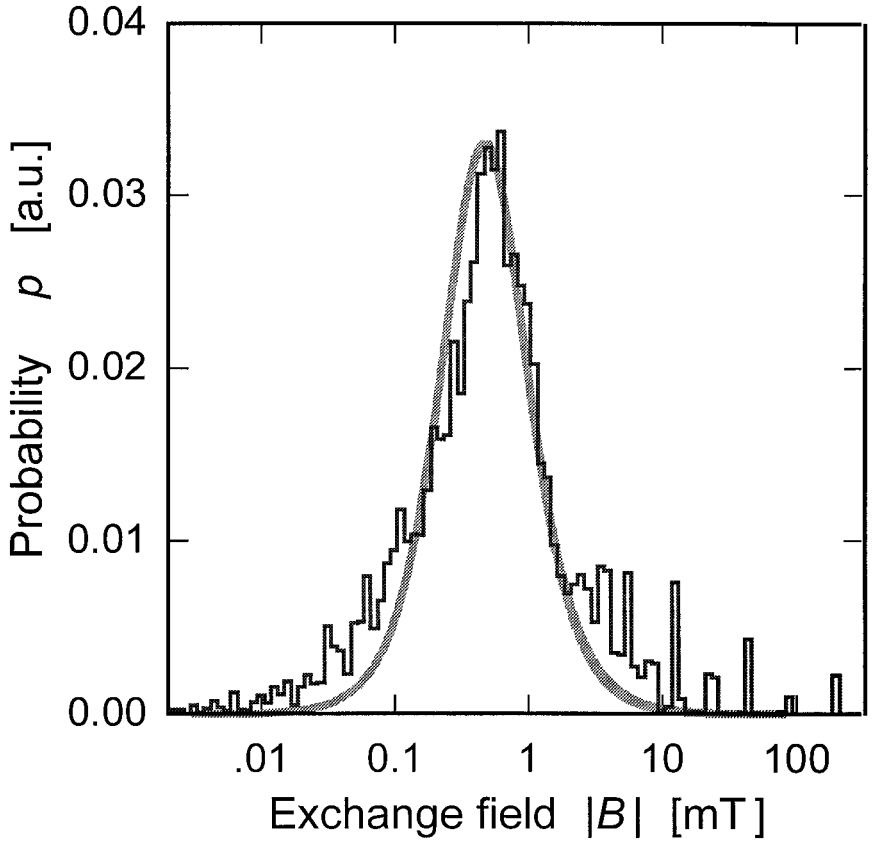


Fig.1. A histogram of the probability distribution of exchange fields of a sample with 300 ppm Er randomly distributed on the fcc Au lattice due to the RKKY interaction under the condition that  $g\mu_B < k_B T$ . The curve is the distribution calculated from Eq. (7) for  $\alpha = 1$  and  $B_{\text{ex}} = (\alpha g\mu_B / 4a_0^3) h$ .

where  $\delta h = 8\pi x/3$ ,  $x$  being the concentration of spins, and the exchange energy for a pair of spin 1/2 ions in terms of  $h$  is given by  $E_{\text{ex}} = (\mu_0/4\pi)(\alpha(g\mu_B)^2/4a_0^3) h$ . The lattice parameter for the fcc Au lattice is  $a_0$ . The expression given by Eq. (7) has been shown by Walker and Walsted<sup>9</sup> to be an accurate representation of the probability distribution of mean fields for random spins located in a continuous medium rather than in discrete lattice sites. In the case that  $g\mu_B B/k_B T < 1$  the thermodynamic properties of interacting spins calculated using the analytical expression Eq. (7) for the exchange energy distribution are in very good agreement with those obtained using the distributions determined numerically. Although the calculations differ somewhat in the operating range of  $B$  and

$T$  of interest in this research we discuss, first, the sensitivity of a magnetic calorimeter using the analytical expression for the probability distribution rather than the more cumbersome numerical results.

As a check on the accuracy of the mean field calculation, we have diagonalized the Hamiltonian of a collection of up to 12 spins in the presence of a magnetic field and interacting via dipolar as well as exchange interactions.<sup>10</sup> The spins are randomly distributed onto the fcc lattice sites within a cube of  $13a_0$  on a side. The eigenstates are computed for approximately  $10^4$  different random distributions and the thermodynamic properties are then calculated. The number of spins used in the various distributions is weighted in accordance with the probability of occurrence within the volume for a specific concentration. The calculated properties of Au:Er using this approach differ in minor ways from the results of the numerical mean field calculation, as will be discussed in Section 5.

The response of a magnetic calorimeter is measured by placing the sensor in the coil of a SQUID magnetometer. The change in flux within a circular loop of wire of radius  $r_\ell$  due to a change in magnetization of a material in it can be calculated by determining the flux outside the loop. For a change in magnetization in a sample of volume  $V$  parallel to the axis of the loop the flux change is

$$\delta\phi = \int_0^{2\pi} \int_{r_\ell}^{\infty} r \, d\vartheta \, dr \int_V \mu_0 \delta M \frac{(3 \cos^2 \theta_i - 1)}{(r - r_i)^3} dV_i, \quad (8)$$

where  $r_i$  is the position of the volume element  $dV_i$  and  $\theta_i$  is the angle between the direction of the magnetization and  $r_i$ . A magnetic sensor is likely to be a right circular cylinder. The flux in a loop produced by cylinders of radius  $r = r_\ell$  and  $r = 0.92r_\ell$  obtained by numerically integrating Eq. (8), are plotted in Fig. 2 as a function of half length  $z$ . However, rather than having to perform a numerical integration in the calculations below of sensitivity, we substitute an analytic expression for  $\delta\phi$  that is a reasonable approximation to the numerical result for a cylinder.

For an oblate ellipsoid of revolution with its larger semi-major axes equal to the radius of the loop in which it is placed symmetrically, the flux change is

$$\delta\phi = \mu_0 \pi r_\ell^2 (1 - D) \delta M, \quad (9)$$

where

$$D = \frac{d^2}{d^2 - 1} - \frac{d^2}{(d^2 - 1)^{3/2}} \arctan(d^2 - 1)^{1/2}, \quad (10)$$

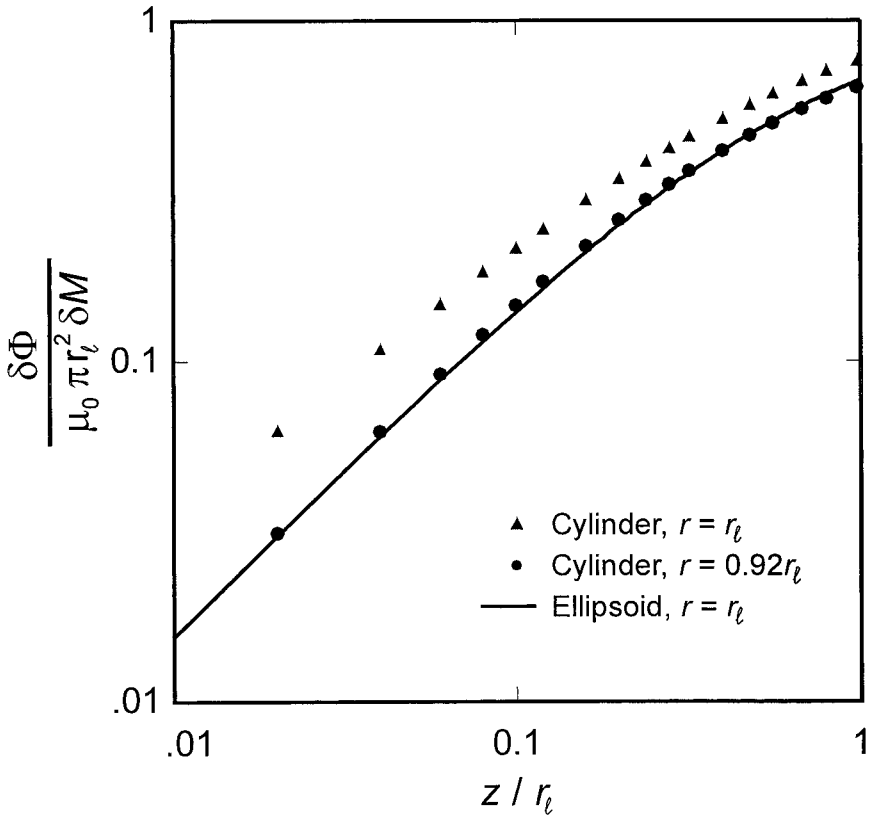


Fig. 2. The flux coupled to a circular loop of radius  $r_\ell$  by cylinders of radius  $r_\ell$  and  $0.92r_\ell$  is plotted as a function of the ratio  $z/r_\ell$  where  $z$  is the half length of the cylinder. Also plotted is the flux coupled to the loop by an oblate ellipsoid with axes  $r_\ell$  and  $z$ .

and  $d = r_\ell/z$  is the ratio of the axes of the ellipsoid of revolution. A plot of  $(1 - D)$  versus  $z/r_\ell$  is shown in Fig. 2. As can be seen, the use of an ellipsoid to calculate analytically the flux produced by a cylinder of the same dimensions is not particularly good. However, the flux calculated for the ellipsoid is within 3% of that of the cylinder with  $r = 0.92r_\ell$  for all values of the ratio  $z/r_\ell$  from 0 to 1. In the region of interest for a magnetic detector,  $0.3 < z/r_\ell < 0.5$ , the agreement is within 1%. Since a magnetic sensor the same size as the loop is unrealistic in practice, we have arbitrarily assumed the cylinder to have a radius of  $0.92r_\ell$  and calculated the flux using Eq. (9) with  $r = r_\ell$ .

The sensitivity, defined as the flux change per unit energy input,

$$S = \frac{\delta\phi}{\delta\varepsilon} = \frac{(\partial\phi/\partial T)}{C_{\text{spin}} + C_a}, \quad (11)$$



is a function of a number of parameters. The total heat capacity of the system is written as the sum of the heat capacity of the spin system,  $C_{\text{spin}}$  (Zeeman plus exchange), and  $C_a$ , that of the x-ray absorber. The heat capacity of the conduction electrons is not explicitly included here, but it is discussed below. When account is taken for the distribution of exchange fields, the temperature dependence of the magnetization and the spin heat capacity are obtained from standard thermodynamic arguments to be

$$\frac{\partial M}{\partial T} = \frac{x N_A g \mu_B}{V_m T} \int dh P(h) \left[ \left( \frac{y_+}{(e^{y_+} + e^{-y_+})^2} \right) + \left( \frac{y_-}{(e^{y_-} + e^{-y_-})^2} \right) \right], \quad (12)$$

and

$$C_{\text{spin}} = \frac{2x N_A V}{V_m} \int dh P(h) \left[ \left( \frac{y_+^2}{(e^{y_+} + e^{-y_+})^2} \right) + \left( \frac{y_-^2}{(e^{y_-} + e^{-y_-})^2} \right) \right], \quad (13)$$

where

$$y_{\pm} = \frac{g \mu_B B \pm \frac{1}{2} \alpha (g^2 \mu_B^2 / a_0^3) h}{2 k_B T}.$$

In Eqs. (12) and (13)  $N_A$  is Avogadro's number and  $V_m$  is the molar volume. We have assumed that the exchange field can either be positive or negative compared to the applied field, thus the two terms, one involving  $y_+$  and the other  $y_-$ .

The sensitivity  $S$  depends upon a number of quantities.

$$S = S(C_a, g, \alpha, T, x, r, z, B). \quad (14)$$

Four parameters—the heat capacity of the absorber  $C_a$ , the  $g$ -factor of the paramagnetic ions, the strength of the RKKY interaction  $\alpha$ , and the operating temperature  $T$ —are generally fixed by the experimental conditions and choice of materials. However, the other four—the concentration of ions  $x$ , the radius  $r$  and length  $z$  of the cylindrically shaped sensor, and the applied magnetic field  $B$ —are adjustable. The values of these latter four parameters can be varied so as to maximize  $S$ . The values of  $x$ ,  $r$ ,  $z$ , and  $B$ , that maximize  $S$  are found numerically to depend upon  $C_a$ ,  $g$ ,  $\alpha$ , and  $T$  as given in Table I. The maximum sensitivity for a given set of parameters is also listed in Table I and is given by

$$S_{\text{max}} = 1.7 \times 10^{-9} \left( \frac{g}{C_a \alpha T^2} \right)^{1/3} \Phi_0 / \text{eV}, \quad (15)$$

where  $\Phi_0 = 2.07 \times 10^{-15}$  Wb is the flux quantum.

TABLE I

The Dependence of the Variable Parameters  $B$ ,  $x$ ,  $r$ ,  $z$ , Upon the Operational Parameters  $C_a$ ,  $T$ ,  $g$ , and  $\alpha$  Such That the Sensitivity  $S$  is Maximized. The Last Column Contains Explicit Values for a Au:Er Sensor ( $g = 6.8$ ,  $\alpha = 5$ ) at 50 mK Connected to an Absorber that has a Heat Capacity of  $C_a = 1 \times 10^{-12}$  J/K.

Optimal parameters	For $g = 6.8$ , $\alpha = 5$ , $T = 0.05$ K, $C_a = 1 \times 10^{-12}$ J/K
$B_{\max} = 1.5 \text{ T K}^{-1} \times T g^{-1}$	$\hookrightarrow 10.9 \text{ mT}$
$x_{\max} = 4.2 \text{ K}^{-1} \times T g^{-2} \alpha^{-1}$	$\hookrightarrow 900 \text{ ppm}$
$r_{\max} = 1.05 \text{ cm} \frac{\text{K}^{2/3}}{\text{J}^{1/3}} \times (C_a g^2 \alpha T^{-1})^{1/3}$	$\hookrightarrow 17 \mu\text{m}$
$z_{\max} = 0.40 \times r_{\max}$	$\hookrightarrow 7.0 \mu\text{m}$
$S_{\max} = 1.7 \times 10^{-9} \frac{\Phi_0}{\text{eV}} \frac{\text{J}^{1/3}}{\text{K}} \times (g C_a^{-1} \alpha^{-1} T^{-2})^{1/3}$	$\hookrightarrow 1.4 \times 10^{-4} \frac{\Phi_0}{\text{eV}}$

In the last column of Table I are listed the numerical values of the parameters for Er in Au at a temperature of 0.05 K with an absorber having a heat capacity of  $10^{-12}$  J/K. To put the calculated sensitivity of  $1.4 \times 10^{-4} \Phi_0/\text{eV}$  in perspective, consider the following. The noise of commercial SQUIDS is typically in the vicinity of  $3 \times 10^{-6} \Phi_0/\sqrt{\text{Hz}}$ . (The noise of state of the art devices may be an order of magnitude lower than this.) With a bandwidth of  $10^3$  Hz, a threshold of  $\sim 1$  eV is conceivable with the operating parameters selected.

Several observations should be made regarding these calculations.

(i) To obtain a value of  $S$  close to its maximum for a particular set of operating parameters,  $C_a$ ,  $T$ ,  $g$ , and  $\alpha$ , it is not critical to set  $B$ ,  $x$ ,  $r$  and  $z$  to precisely their optimal values. If one variable differs from its best value, then the other variables can be adjusted accordingly. Consider again the case with operating parameters  $g = 6.8$ ,  $\alpha = 5$ ,  $T = 0.05$  K and  $C_a = 1 \times 10^{-12}$  J/K. If  $x$  is greater than  $x_{\max}$  by a factor of 2, i.e.,  $x = 2x_{\max}$ , then by changing  $r$  and  $B$  so that  $r = 0.76r_{\max}$  and  $B = 1.4B_{\max}$ , the sensitivity is less than its maximum value by only 4%.

(ii) The value of  $B_{\max}$  is such that  $g\mu_B B_{\max}/k_B T \approx 1$ . Since the Zeeman splitting is comparable to  $k_B T$ , the thermodynamic properties of the system determined using the analytic distribution  $P(h)$  of Walker and Walsted<sup>9</sup> are in some error. In selected cases we have used the numerical probability distribution of the exchange energy to calculate the conditions for maximum sensitivity. The sensitivity  $S$  is found to be approximately 10% higher than obtained using Eq. (15). The values of  $x$ ,  $B$  and  $r$  that

maximize  $S$  differ from those given above by  $\sim 15\%$ . However, the functional dependence of  $x$ ,  $B$  and  $r$  upon  $C_a$ ,  $T$ ,  $g$ , and  $\alpha$  given above remains a reasonably good approximation.

(iii) Because the sensitivity of an optimally designed magnetic calorimeter depends only weakly on the heat capacity of the absorber, i.e., as  $C_a^{-1/3}$ , this type of device should prove very useful in calorimeters with large heat capacity. The signal is maximized when  $C_{\text{spin}} = C_a$ , and since both  $B$  and  $x$  are independent of  $C_a$ , the volume of the sensor, proportional to  $r^2 z$ , varies as  $C_a$ . Insofar as  $C_a$  decreases with temperature, the sensitivity varies more rapidly with temperature than  $T^{-2/3}$ .

(iv) In general, with  $x$  and  $r$  fixed but  $C_a \propto T$ , the absolute value of the logarithmic derivative,  $d \ln S / d \ln T$ , of the sensitivity with respect to temperature is close to unity. The temperature stability required to achieve a given energy resolution is therefore not as stringent as with some other sensors, e.g., thermistors.

(v) The magnitude of the reduction in sensitivity caused by the RKKY exchange interaction depends upon the operating conditions. At 0.05 K and conditions that maximize  $S$ , the exchange primarily reduces the temperature dependence of the magnetization. The heat capacity of the spins is mainly that of the Zeeman interaction and is changed relatively little by the exchange. The value of  $(\partial M / \partial T)$  is 27% less than the Curie value for noninteracting spins while the heat capacity is only 3% greater.

(vi) In these calculations we have not considered explicitly the influence of the electronic heat capacity,  $C_e$ , of the magnetic sensor. For  $g = 6.8$  and  $\alpha = 5$ , the optimal concentration and size of the sensor is such that the electronic heat capacity is 4% of the heat capacity of the spins, independent of  $T$  and  $C_a$ . (The lattice heat capacity of Au at 0.05 K is more than an order of magnitude smaller than the electronic component and can be neglected.) When  $C_e$  is included in the calculations,  $S_{\text{max}}$  is reduced by 2%, while  $r_{\text{max}}$  is reduced by 10%,  $B_{\text{max}}$  is increased by 12%, and  $x_{\text{max}}$  is increased by 20%.

(vii) We have assumed that a loop of radius  $r_\ell$  surrounds the mid-point of a cylinder of radius  $0.92r_\ell$ , the length of the cylinder being  $2z$ . In a real device it is likely that the magnetic sensor will be deposited within the loop, which with its SQUID is fabricated on a substrate. In this geometry, the loop is at one end of the cylinder rather than at the middle. Then the optimal radius is larger by a factor of  $2^{1/3}$ ,  $z = 0.40r$  is, in this case, the length of the cylinder rather than the half length, and the sensitivity is smaller by the same factor of  $2^{1/3}$ .

(viii) Hyperfine interactions can have a major effect on the sensitivity of a magnetic calorimeter. The 23% abundant isotope  $^{167}\text{Er}$  with nuclear spin  $7/2$  has a zero-field energy splitting between the  $F=4$  and  $F=3$  multiplets of 0.134 K. At 0.05 K this hyperfine interaction results in a large heat capacity and substantially reduces the sensitivity. At lower temperatures where only the lower  $F=3$  multiplet is appreciably occupied, the effect is different. The projection of electronic spin onto a state characterized by  $m_F$  is small. The effective  $g$ -factor of the  $F$  multiplet is much lower ( $\approx \frac{1}{4}g$  at low fields) than that of the electronic ground state. As a consequence, the magnetization is reduced as is the RKKY interaction involving a  $^{167}\text{Er}$  ion. The net effect of the hyperfine interaction is to decrease the sensitivity, and it is best to work with paramagnetic ions having zero nuclear moment.

(ix) We have associated the maximum sensitivity of a magnetic calorimeter with the maximum flux change in a SQUID loop. The diameter of the loop and the sample within it are variable. This implicitly assumes that the inductance of the loop is of no consequence in determining the sensitivity. The assumption is valid so long as the flux noise of the SQUID limits the performance of the system, a condition that is satisfied in the measurements reported here. With SQUIDs having lower noise so that other noise sources dominate, such as those discussed below, the conditions for optimization are much different. The functional dependence of the variable parameters upon the operating conditions will be not be those listed in Table I. The optimal size of the sample and loop will be smaller while the concentration and magnetic field will be larger than calculated here.

### 2.3. Relaxation Times

Because of the strong interaction between the localized spins and conduction electrons in a metal, a metallic magnetic sensor responds rapidly at low temperatures when energy is deposited within it. The time constant for exchange of energy between Er ions and conduction electrons in Au is known from the temperature dependence of the width of the spin resonance line.<sup>11</sup> Lifetime broadening of the Er resonance is observed even below 1 K.<sup>12</sup> The relaxation time,  $T_1$ , between Er ions and conduction electrons obeys the Korringa relation  $T_1 T = K$  where  $K = 7 \times 10^{-9} \text{ sK}$ . Once the energy deposited in an absorber is transferred to the sensor via conduction electrons, the spins will register that energy in less than  $10^{-6} \text{ s}$  at 50 mK. The response time of the calorimeter is not determined by the spin-electron relaxation time but rather by the coupling of the absorber to the sensor. The return of the temperature of the calorimeter to that of the reservoir is dependent on the thermal coupling between the two.

The process by which the energy of an x-ray is transformed into thermal excitations within a metallic absorber appears not to have been fully described in the literature. The initial energetic electron, produced by photoelectric absorption of the x-ray, quickly loses energy by interactions with other electrons. The de-excitation of the ion from which the photoelectron was ejected may produce other energetic electrons. The electron-electron scattering time for an electron having energy  $E$  above the Fermi surface  $\varepsilon_F$  with electrons in the Fermi sea is<sup>13</sup>

$$\tau_{ee} = \tau_0 \left( \frac{\varepsilon_F}{E} \right)^2, \quad (16)$$

where

$$\tau_0 = \frac{128}{\sqrt{3} \pi^2 \omega_p} \approx 5 \times 10^{-16} \text{ s (for Au)}, \quad (17)$$

and  $\omega_p$  is the plasma frequency.<sup>14</sup> As a consequence of repeated scattering, after a time  $t$  the energy of the x-ray is distributed over a large number of electrons with average energy<sup>15</sup>

$$\langle E \rangle = 0.38 \left( \frac{\tau_0}{t} \right)^{1/2}. \quad (18)$$

At some time the average energy of the excited electrons has decreased sufficiently that phonon emission dominates the thermalization process.<sup>15</sup> Lifshitz *et al.*<sup>16</sup> have shown that if an electron has energy large compared to the Debye energy, it loses energy by interaction with phonons at the rate

$$\dot{q} = \frac{\pi \hbar \lambda \langle \omega^2 \rangle}{2 \ln 2}, \quad (19)$$

where  $\lambda$  is the electron-phonon coupling parameter and  $\langle \omega^2 \rangle$  is the average of the square of the phonon frequency. For Au  $\lambda = 0.15$ ,<sup>17</sup> and with  $\langle \omega^2 \rangle^{1/2} \approx \omega_{\text{Debye}}$ , the time at which phonon emission becomes a greater loss mechanism than electron scattering is roughly  $10^{-13} \text{ s}$   $\lambda$  and the average electron energy is 0.1 eV. After phonon emission becomes dominant, much of the energy of the x-ray is transferred to the phonon system. The high frequency phonons, in turn, interact with electrons in the Fermi sea and lose energy. The energy must eventually return to the electron system since the heat capacity of the conduction electrons is much larger than that of the lattice below 1 K. The time scale for this evolution has not been worked

out in detail.<sup>18</sup> However, in a normal metal the time is likely to be sufficiently short that it is not of relevance to the design features of an absorber for a magnetic calorimeter. What is more important are the processes that occur once the electrons in a region of a few microns about the location of the x-ray absorption have reached a temperature below 1 K. The diffusion of this energy throughout the absorber and to the sensor, governed by electron scattering from defects, grain boundaries, impurities, etc. will determine the response of the calorimeter. The time for diffusion should be the order of  $10^{-6}$  s for an Au absorber having dimensions of 1 mm.

## 2.4. Noise

Ultimately, what limits the energy resolution and threshold of a magnetic calorimeter is the noise in the device. In addition to noise due to electromagnetic pick up, microphonics, and the electronics, there are several intrinsic noise sources. Intrinsic noise arises from the dc SQUID itself, from thermodynamic variation in the energy content of the calorimeter because of its coupling to a reservoir, and from fluctuating currents in conductors in the vicinity of the pick up coil and SQUID. The fluctuating currents generate flux noise in the pick up circuit which is often called magnetic Johnson noise. While magnetic Johnson noise is not a contributing factor in the present measurements, we discuss it in some detail below since it will become important for detectors having metals in the vicinity of the magnetic calorimeter and for which other noise sources have been reduced.

### 2.4.1. SQUID Noise

The intrinsic flux noise in an optimally designed dc SQUID will depend upon the inductance of the circuit containing the junctions. For a SQUID with an inductance of 100 pH the flux noise should approach  $10^{-7} \Phi_0/\sqrt{\text{Hz}}$ .<sup>19</sup> At a time when a such low-noise SQUID is used in conjunction with a magnetic calorimeter, then the performance characteristics and optimization conditions of the coupled SQUID/calorimeter system must be analyzed afresh. Currently, with dc SQUIDs having a flux noise of a few  $\mu\Phi_0/\sqrt{\text{Hz}}$ , independent of the inductance of the circuit, this complexity is irrelevant.

### 2.4.2. Magnetic Johnson Noise

We discuss magnetic Johnson noise in the context of the detector design in which the magnetization of a thin disc of material is sensed by a loop within the ring of a two-junction dc SQUID. In that design, magnetic

Johnson noise can be produced by the metallic sensor in which the paramagnetic ions are embedded, the metallic foil used for absorbing x-rays, and also by metallic materials used for construction, thermal conduction or electromagnetic shielding in the immediate vicinity of the detector.

A number of authors<sup>20, 21</sup> have calculated the fluctuations in magnetic field arising from the thermal currents in a conductor starting from the random motion of the charges. Alternatively, as pointed out by Harding and Zimmerman,<sup>22</sup> the flux noise generated in a coil or loop as a consequence of fluctuating currents in a conductor can be calculated using the reciprocity theorem. A time-varying current at frequency  $\omega$  in a coil produces eddy currents in nearby conductors, and the resulting losses can be described by an apparent resistive impedance  $R(\omega)$  of the coil. This impedance can then be used to deduce the flux noise in the coil or loop. Since the voltage across a superconducting coil and the flux through it are related simply by  $V(\omega) = \omega \phi(\omega)$ , the rms flux noise per root Hertz is

$$\sqrt{\mathcal{S}_\phi} = \frac{1}{\omega} \sqrt{\mathcal{S}_V} = \left( 4\pi k_B T \frac{R(\omega)}{\omega^2} \right)^{1/2}. \quad (20)$$

The components of the magnetic field at position  $(\rho, z)$  in cylindrical coordinates produced by a current  $I(\omega)$  in a circular loop of wire of radius  $a$ , the center of which is at the origin, are in mks units,<sup>23</sup>

$$B_\rho = \frac{\mu_0 I(\omega)}{4\pi} \frac{2z}{\rho[(a+\rho)^2 + z^2]^{1/2}} \left[ -K(k) + \frac{a^2 + \rho^2 + z^2}{(a-\rho)^2 + z^2} E(k) \right], \quad (21)$$

and

$$B_z = \frac{\mu_0 I(\omega)}{4\pi} \frac{2}{[(a+\rho)^2 + z^2]^{1/2}} \left[ K(k) + \frac{a^2 - \rho^2 - z^2}{(a-\rho)^2 + z^2} E(k) \right], \quad (22)$$

where  $K(k)$  and  $E(k)$  are complete elliptic integrals of the first and second kind with

$$k^2 = 4a\rho[(a+\rho)^2 + z^2]^{-1}. \quad (23)$$

We consider, first, a conducting sheet with conductivity  $\sigma$  and thickness  $t$  small compared to the skin depth,  $\xi = \sqrt{2/\mu_0 \sigma \omega}$ . If the sheet is parallel to the plane of the loop of wire and separated from it by a distance  $z$ , then the eddy current density is given by

$$i = \frac{\mu_0 \omega \sigma I(\omega)}{8\pi^2} \frac{\eta(a, z, r)}{r} \quad (24)$$

where

$$\eta(a, z, r) = 2\pi \int_0^r \frac{1}{[(a+\rho)^2 + z^2]^{1/2}} \left[ K(k) + \frac{a^2 - \rho^2 - z^2}{(a-\rho)^2 + z^2} E(k) \right] \rho d\rho. \quad (25)$$

The power dissipated in an infinite sheet by the eddy currents is

$$P = \int \frac{1}{\sigma} i^2 dV = \frac{\mu_0^2 \sigma \omega^2 I^2(\omega) t}{32\pi^3} \int_0^\infty \frac{\eta^2(a, z, r)}{r} dr. \quad (26)$$

The integral involving  $\eta$  can be shown to be  $(\pi^4 a^4 / z^2)$  so that the effective impedance of the loop due to the presence of the conductor is

$$R(\omega) = P/I^2 = \frac{\mu_0^2 \sigma \omega^2 t}{32\pi z^2} (\pi a^2)^2, \quad (27)$$

and the spectral flux noise density in the loop is

$$\sqrt{\mathcal{G}_\phi} = \left( \frac{\mu_0^2 \sigma k_B T t}{8\pi z^2} \right)^{1/2} (\pi a^2). \quad (28)$$

This expression is exactly the same as can be obtained from the results of Varpula and Poutanen<sup>20</sup> and of Gillespie<sup>21</sup> for an infinite sheet in the low frequency limit where the skin depth is larger than the thickness of the conductor.

The geometry of interest for magnetic sensors is a disk of radius  $r$  and thickness  $t$  inside a loop of radius  $a$ . In this case  $z=0$  in the expression for  $\eta$ . The upper limit of the integral in Eq. (26) is now  $r$ , and the value of the integral is  $(\pi^4 r^4 / a^2) \mathcal{C}$ , where the numerical coefficient  $\mathcal{C}$  is 1 for small values of  $r/a$ , increases slowly with increasing  $r$  reaching the value of 1.5 at  $r/a=0.8$  and the value of 2.2 at  $r/a=0.95$ . At  $r=a$  the integral in Eq. (26) is infinite. The spectral flux noise density for a disc within the loop is then

$$\sqrt{\mathcal{G}_\phi} = \mathcal{C}^{1/2} \left( \frac{\mu_0^2 \sigma k_B T t}{8\pi a^2} \right)^{1/2} (\pi r^2). \quad (29)$$

We have not calculated the magnetic Johnson noise using the reciprocity theorem at high frequencies where a metal is thicker than the skin depth since in this situation it is not possible to express the noise for a cylinder in analytical form. Instead, we compute the noise numerically using the results of Varpula and Poutanen.<sup>20</sup> The Johnson noise rolls off with increasing frequency in this regime.



### 2.4.3. Thermodynamic Energy Fluctuations

The internal energy of any thermodynamic system with heat capacity  $C$  coupled to a thermal reservoir will fluctuate with a frequency dependence given by

$$\mathcal{S}_E(\omega) d\omega = \frac{2}{\pi} (k_B T^2 C) \frac{\tau d\omega}{1 + (\omega\tau)^2}, \quad (30)$$

where  $\tau$  is the time constant for the system to establish thermal equilibrium with the reservoir. The rms energy fluctuation is then

$$\langle (\delta E)^2 \rangle^{1/2} = \sqrt{k_B T^2 C}. \quad (31)$$

For a calorimeter with a heat capacity of  $1 \times 10^{-12}$  J/K at 0.05 K, the rms energy fluctuation is 1.2 eV while for  $C = 1 \times 10^{-9}$  J/K, it is 37 eV. However, the performance characteristics of a calorimeter are not necessarily limited by the rms energy fluctuations. By restricting the frequency domain in which the measurements of energy are made the fluctuations can be reduced below the rms value. Measurements can be performed in a time short compared to the time scale in which thermal fluctuations occur.

## 3. EXPERIMENT

### 3.1. Sample Preparation

The starting material for our Au:Er sensors was 5 N gold.<sup>24</sup> Alloys were prepared by arc melting in an argon atmosphere using either natural Er or isotopically enriched Er, 97.2% spin-zero isotopes, 2.8% <sup>167</sup>Er.<sup>25</sup> A master alloy of 1% Er was made first, and then samples of 100 to 2000 ppm were prepared by further dilution with pure Au. Alloys were repeatedly arc melted from five to eight times to reduce inhomogeneities.

The Er concentrations were determined experimentally by measuring the magnetization of the samples from 1.4 to 300 K in fields of 1 to 4 Tesla.<sup>8</sup> In all samples the magnetic measurements gave an Er concentration approximately 25% lower than expected from the ratio of starting materials.

A gold sample with no Er added was arc melted and treated in the same manner as the alloys. Its magnetization measured before arc melting was found to be the equivalent of 0.5 ppm Er. After arc melting the magnetization was the equivalent of 1 ppm Er. The gold was also checked by neutron activation analysis for possible Fe contamination. No Fe was detected setting an upper limit on the concentration of 3 ppm.

### 3.2. Calorimeter Design

We have used two differently designed magnetometers to measure the flux change in an Au:Er sensor upon the absorption of an x-ray. In one magnetometer the flux change in the sensor is coupled to a commercial SQUID using a superconducting flux transformer. In the second design, the magnetic sensor is placed directly within a loop that forms part of the ring of a dc SQUID. It is this latter geometry for which the calculations of sensitivity and noise have been performed.

A schematic diagram of the magnetometer employing a superconducting transformer is shown in Fig. 3a). A cylindrical Au sample with a concentration of 480 ppm of natural Er had a diameter of 0.36 mm and length of 0.5 mm. It was wrapped with 32 turns of 35  $\mu\text{m}$  diameter niobium wire. This sample coil was connected to the input transformer coil of a SQUID located 50 cm away. The estimated efficiency of transfer of flux from the sample coil to the SQUID was 30%. No separate absorber was attached to the magnetic sensor. The x-rays from either a  $^{57}\text{Co}$  or a  $^{55}\text{Mn}$  source were absorbed directly in the sensor. The sensor is more than 80% efficient in absorbing the 122 keV  $\gamma$ -rays from the Co source. The Au:Er sample was spot welded to a copper block, which served as a thermal reservoir. The block was, in turn, thermally attached to a plate cooled by the mixing chamber of a dilution refrigerator.

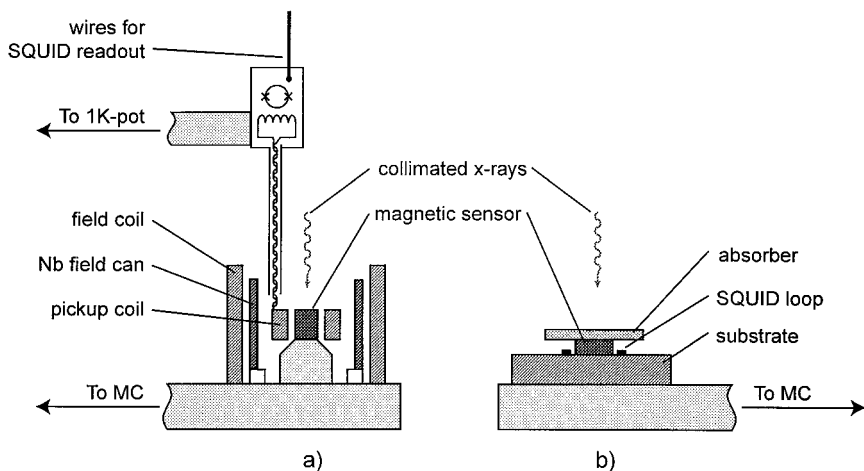


Fig. 3. Schematic diagram of the magnetometer setups. (a) The flux change of the sample is coupled to a dc SQUID via a superconducting transformer. (b) The sample is placed in a loop that is part of the dc SQUID circuit.

In the second design, the circuit containing the SQUID junctions was expanded to include a circular loop of  $50\text{ }\mu\text{m}$  diameter,<sup>26</sup> see Fig. 3b). A laser cut sample of Au:Er,  $50\text{ }\mu\text{m}$  diameter and  $25\text{ }\mu\text{m}$  thick, was placed inside the loop and held there with a small amount of vacuum grease. The Er, in a concentration of 300 ppm, was depleted in  $^{167}\text{Er}$ . In one set of experiments, no separate absorber was attached and the x-ray were stopped in the magnetic sensor itself. In another set a  $100\text{ }\mu\text{m}$  square foil of high purity Au,  $8\text{ }\mu\text{m}$  thick served as the x-ray absorber. It was attached to the magnetic sensor using a wedge bonder. The foil is 100% efficient in absorbing 6 keV x-rays from a  $^{55}\text{Mn}$  source. The chip containing the SQUID and sensor was cooled by attaching it to a plate in thermal contact with the mixing chamber.

With both magnetometers, the magnetic field was applied to the sensor using a superconducting niobium cylinder. The field was trapped in the cylinder by cooling the niobium through its superconducting transition in an externally applied field. In the magnetometer where the magnetic sensor is within the SQUID loop, the junctions are also within the field. In this case the magnetic field could not be increased above about 3.5 mT without producing excess noise.

### 3.3. Temperature Regulation

A schematic diagram of the apparatus used for regulating temperature of the single-loop magnetometer is illustrated in Fig. 4. The micro-calorimeter is attached to a copper plate (P1), which is weakly connected thermally to a second thermal stage (P2). This stage is weakly connected thermally to the mixing chamber (MC) of a dilution refrigerator capable of reaching 5 mK. The temperature of the mixing chamber can be stabilized to  $50\text{ }\mu\text{K}$  using a heater controlled by a carbon thermometer. The plate P2 has on it an additional heater and thermometer.

This thermometer is based on the measurement of the magnetization of a 300 ppm Au:Er cylindrical sample, 0.4 mm diameter, 0.5 mm long, in an applied field of 2 mT with a commercial SQUID. The temperature resolution of the thermometer at 20 mK is better than  $10\text{ nK}/\sqrt{\text{Hz}}$ . With this thermometer the temperature of the plate was regulated to  $0.1\text{ }\mu\text{K}$  on a time scale of minutes. The long-term drift was less than  $1\text{ }\mu\text{K}$  per hour.

Measurements with the large calorimeter were performed without the thermal stage P2 and the temperature regulation it provided.

### 3.4. Signal Analysis

The signal pulses resulting from the absorption of an x-ray are digitized by a 12 bit AD converter and transferred to a computer. Typically

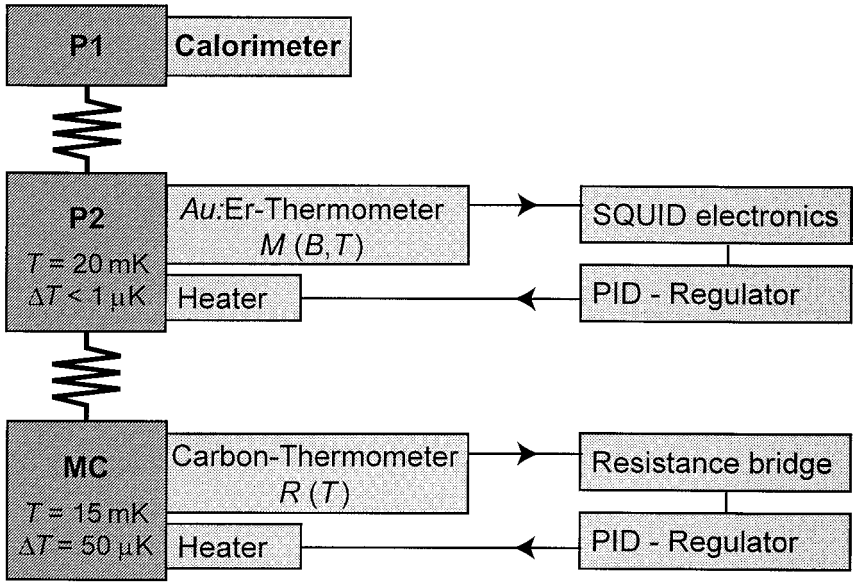


Fig. 4. Schematic diagram of apparatus used for temperature regulation.

16 k samples are acquired per trace, and limitations on the electronics constrained pulse acquisition rates to a few hundred per second. The time window in which the signal is recorded is set so that roughly one quarter of the samples are obtained before the arrival of the pulse. A pulse is rejected if it is delayed by less than 5 time constants associated with the sensor returning to thermal equilibrium. An analog pulse-shaping amplifier is not employed, since to use such a device would render features of the pulses, discussed in the next section, unobservable.

The pulses acquired are averaged to form a template, and then the mean squared deviation of each pulse with respect to the template is minimized to determine its relative size using the relation

$$A = \frac{\langle sa \rangle - \langle s \rangle \langle a \rangle}{\langle a^2 \rangle - \langle a \rangle^2} \quad (32)$$

where  $\langle x \rangle = (1/N) \sum_i x(t_i)$ . The quantities  $s(t_i)$  and  $a(t_i)$  are the signal and template amplitudes, respectively, at time interval  $t_i$ .

The contribution of random noise to the linewidths of the x-ray lines can be separated from other systematic sources of broadening. Randomly

triggered baseline traces are recorded that contain no pulse signal. The replacement of the signal pulses  $s(t_i)$  in Eq. (32) by the baseline traces produces a distribution about zero amplitude that reflects the contribution of random noise to the linewidth.

In determining the energy resolution of the calorimeters, the amplitude of the signals had to be limited to less than  $0.4\Phi_0$  although in some cases the pulse height was as much as  $1.5\Phi_0$ . The slew rate of the SQUID electronics was not fast enough for the feedback circuit to maintain the SQUID locked to a given flux state when the signal was large.

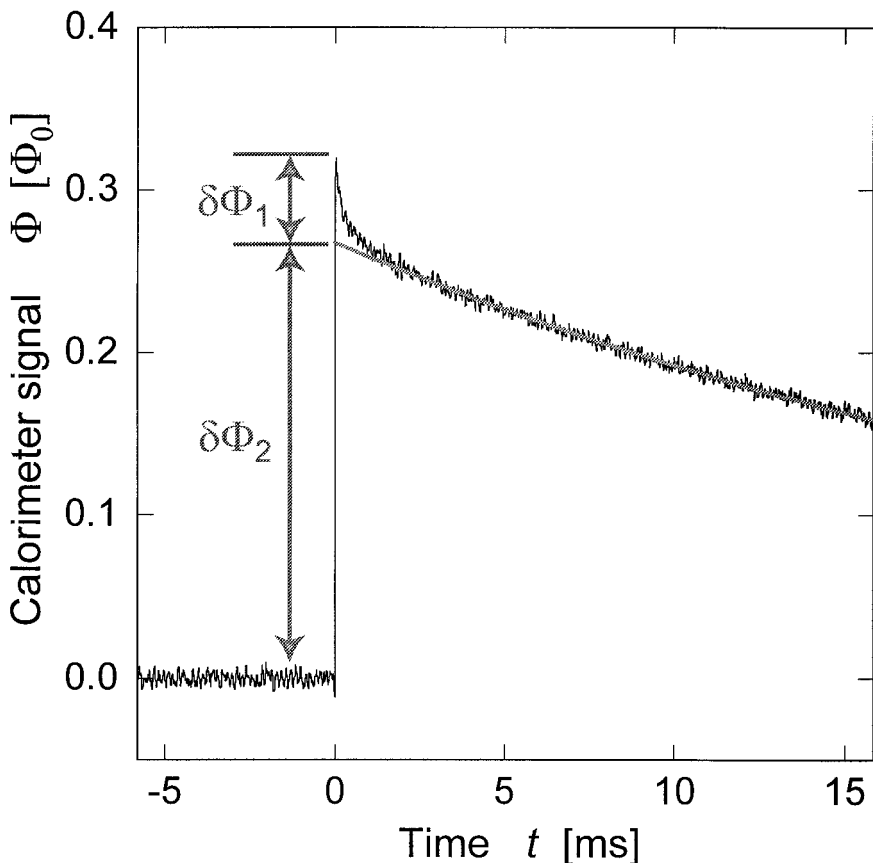


Fig. 5. A typical pulse recorded using the large magnetometer. The pulse, taken at 47 mK, exhibits two exponential decays as the sample returns to thermal equilibrium. In this measurement the sensor was attached to the copper block with varnish rather than by spot welding so as to increase  $\tau_2$ .

## 4. RESULTS AND DISCUSSION

### 4.1. Detector Performance

When an x-ray is absorbed in an Au:Er magnetic calorimeter above a temperature of 80 mK, the flux change exhibits a standard pulse shape with a rise time of approximately  $10\ \mu\text{s}$  determined by the electronics and a single exponential fall time characteristic of the return of the calorimeter to the temperature of the reservoir. As the temperature is decreased below 80 mK, the decay of the pulse can no longer be described by a single exponential but rather requires two exponentials for a fit,

$$\delta\phi = \delta\phi_1 e^{-t/\tau_1} + \delta\phi_2 e^{-t/\tau_2}. \quad (33)$$

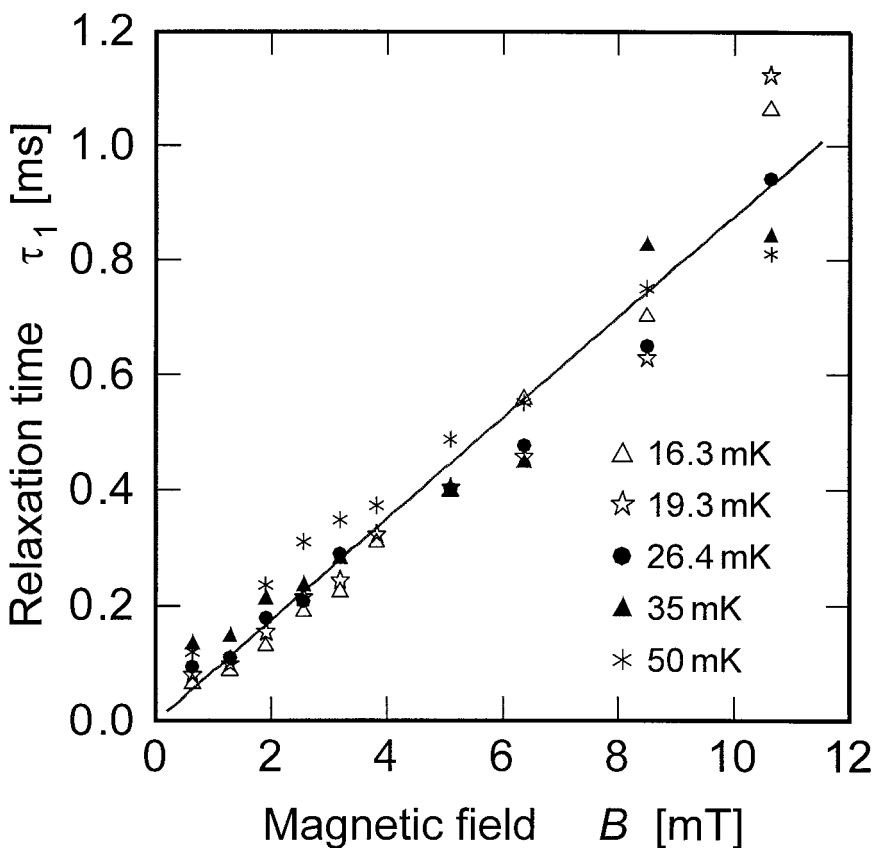


Fig. 6. The field dependence of the time constant  $\tau_1$  measured at several temperatures.

The decay illustrated in Fig. 5 was observed in Au:Er samples of several concentrations and in both magnetometer designs. The longer of the two decays, having the time constant  $\tau_2$ , is the equilibration time for the calorimeter with the reservoir. The existence of the shorter time constant  $\tau_1$  in our metallic magnetic calorimeter is not related to observations of a similar nature with superconducting transition edge sensors or semiconducting thermistors attached to dielectric absorbers. In those cases the initial fast decay is related with the arrival of athermal phonons. Athermal phonons would not couple more strongly to the magnetic ions than to the conduction electrons. Rather, the fast decay indicates the presence of a subsystem with significant heat capacity in the calorimeter that, immediately after the energy deposition, is not in thermal equilibrium with the Zeeman system. We discuss the likely origin of this additional heat capacity below in the section on the properties of Au:Er. The fact that the decay of the

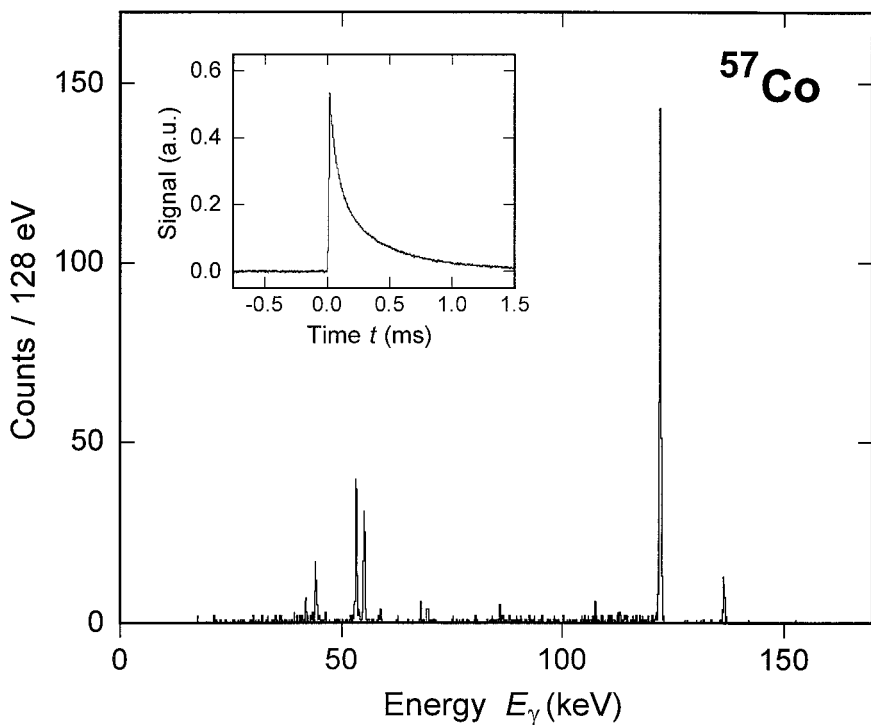


Fig. 7. The spectrum of  $^{57}\text{Co}$  as observed in the large calorimeter. In addition to the standard lines, escape peaks are observed. The energy scale is calibrated using the 122 keV line. The inset shows a single pulse from a 122 keV absorption.

signal is not a simple exponential does not effect the analysis of the pulse to determine the energy of the x-ray that produced it.

The field dependence of  $\tau_1$  is plotted in Fig. 6. There is no measurable temperature dependence to  $\tau_1$  given the scatter in the data. A measured field dependence of  $\tau_2$ , which is not shown since it contains no additional information, is due entirely to the field dependence of heat capacity associated with the Zeeman interaction. The thermal conductance,  $G$ , between the sensor and thermal reservoir is calculated from  $G = C_{\text{spin}}/\tau_2$  to be independent of magnetic field, as expected.

The hard x-ray spectrum<sup>27</sup> obtained with the large cylindrical sensor exposed to a  $^{57}\text{Co}$  source at 25 mK and 4.7 mT is shown in Fig. 7. In addition to the 122 keV and 136 keV lines from  $^{57}\text{Co}$ , the spectrum exhibits a

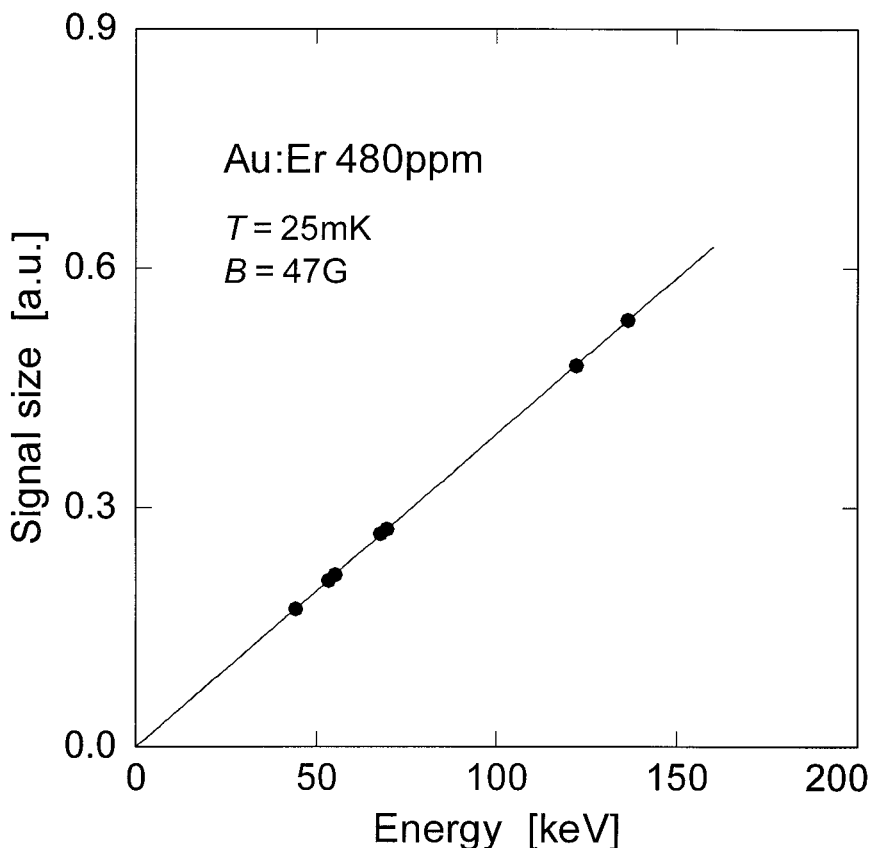


Fig. 8. A plot of pulse height vs. energy for the lines observed in the  $^{57}\text{Co}$  spectrum.



number of escape peaks at lower energies. The efficiency of this calorimeter is greater than 80 % at 122 keV. At the operating conditions of the measurement, the calorimeter had a heat capacity of  $4 \times 10^{-9}$  J/K, due primarily to the magnetic spins.

The temperature rise resulting from the absorption of a 136 keV x-ray is  $5 \mu\text{K}$ , or a fractional temperature rise of  $\delta T/T \simeq 2.5 \times 10^{-4}$ . The calculated nonlinearity of signal size versus energy at this input level is less than 1 part in  $10^5$ . No deviation of signal size versus energy was expected or observed in the data, see Fig. 8. The time constant of the sample, spot welded to a copper block, was less than 1 ms at 20 mK. The measured resolution at 122 keV was 340 eV FWHM. This result was limited by the lack of sufficient temperature regulation. In a separate experiment this calorimeter was exposed to a  $^{55}\text{Mn}$  5.9 keV source where a resolution of 120 eV, limited by electromagnetic pick up, was obtained.

Results obtained with the smaller detector having the  $100 \mu\text{m}$  square,  $8 \mu\text{m}$  thick Au foil attached as an x-ray absorber are shown in Fig. 9. The  $2 \times 10^4$  events associated with the  $K_\alpha$  line of Mn that comprise this spectrum were recorded in 1 h.<sup>28</sup> The operating temperature was 33 mK and the magnetic field was 3 mT. When the observed  $K_\alpha$  line is deconvolved into its known components from the data of Hölzer *et al.*,<sup>29</sup> an instrumental resolution of 12 eV is obtained.<sup>30</sup> As expected, the resolution was unchanged with the absorber removed and the x-rays incident directly on the Au:Er sensor. The heat capacity of the Au absorber at 33 mK is  $5 \times 10^{-13}$  while the heat capacity of the Au:Er sensor in 3 mT is  $1 \times 10^{-12}$  J/K. The time constant of the calorimeter, held in place in the SQUID loop by grease, was about 15 ms.

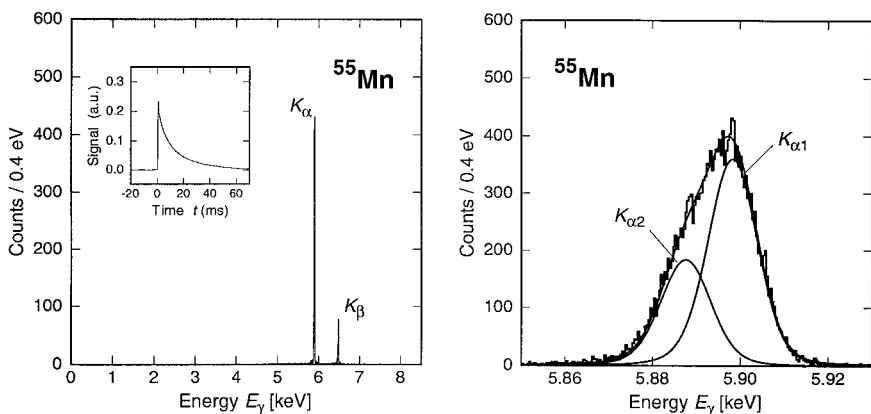


Fig. 9. (a) The spectrum of  $^{55}\text{Mn}$  taken with the small calorimeter. (b) The  $K_\alpha$  line of the spectrum, when deconvolved into its components, shows an instrument half width of 12 eV.

These results at 122 keV and 6 keV bear little relation to the calculated sensitivity of a calorimeter designed for optimal performance. However, the measured size of the signals obtained with both calorimeters agrees within 20% of the response calculated from the known thermodynamic properties of Au:Er. The factor of 20% is consistent with uncertainties in the geometry of the calorimeters and the coupling of the flux to the superconducting coils.

## 4.2. Noise

We discuss only the noise observed in the small, single-loop calorimeter. The noise originates from a number of sources. The SQUID with its electronics contributed white noise of  $4 \mu\Phi_0/\sqrt{\text{Hz}}$  between a  $1/f$  knee at 5 Hz and  $10^5$  Hz where it rolled off due to the circuit response. Electromagnetic pick up and mechanical vibrations introduced noise at several discrete frequencies between 5 Hz and 250 Hz. At low temperatures these sources dominate and limit the energy resolution of the calorimeter.

At high temperatures magnetic Johnson noise is clearly present and distinguishable by its temperature dependence. The temperature dependence of the Johnson noise at 10 kHz is shown in Fig. 10. The calorimeter in this measurement was the 50  $\mu\text{m}$  diameter Au:Er magnetic sensor with the 100  $\mu\text{m}$  square Au absorber attached. Several metallic pieces in the vicinity of the SQUID loop potentially could contribute to the observed Johnson noise. These include a copper sheet used to make thermal contact between the SQUID chip and the copper plate, the magnetic sensor within the SQUID loop and the gold foil used as the x-ray absorber. Of these three metals, the gold absorber is calculated to produce the greatest flux noise because of its high conductivity.

To calculate the flux noise produced by the absorber, we approximate its shape as a 100  $\mu\text{m}$  diameter disc and take the residual resistivity of the gold (5N) to be  $1 \times 10^{-8} \Omega \text{ cm}$ . The plane of the absorber is 25  $\mu\text{m}$  above the 50  $\mu\text{m}$  diameter loop. The flux noise computed with the upper limit of Eq. (26) set at 50  $\mu\text{m}$  is  $3 \times 10^{-5} \Phi_0/\sqrt{\text{Hz}}$  at 4 K. This noise level, and its temperature dependence, is consistent with the observations presented in Fig. 10 at 10 kHz.

Although the Au:Er magnetic sensor is directly within the loop, it produces less Johnson noise than the absorber. The residual resistivity of gold as a function of erbium concentration has been measured<sup>32</sup> and found to be  $\rho = 6.7 \times 10^{-4} \times x \Omega \text{ cm}$  where  $x$  is the fractional concentration of Er. For the 300 ppm sample  $\rho = 0.2 \mu\Omega \text{ cm}$ . For a disc having a radius slightly less than that of the loop of 25  $\mu\text{m}$ , and a thickness of 25  $\mu\text{m}$ , the rms flux noise in the loop, calculated using Eq. (29) at 50 mK and at low frequency,

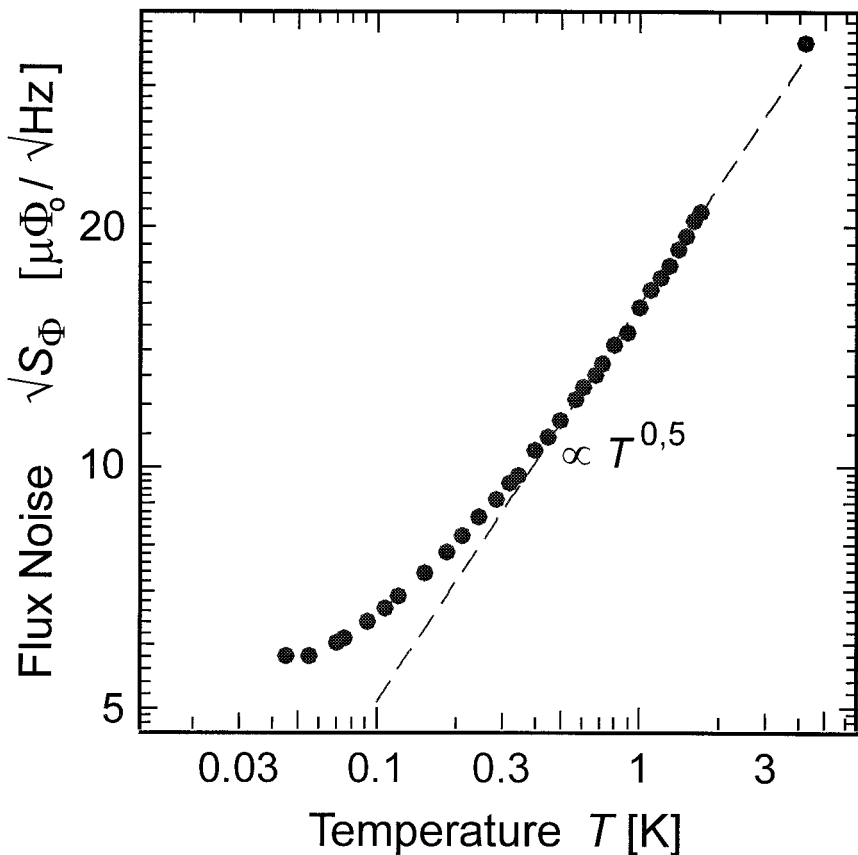


Fig. 10. A plot of the temperature dependence of the noise at 10 kHz observed with the single-loop calorimeter with the Au absorber attached to the magnetic sensor. The line through the high temperature data points is proportional to  $T^{0.5}$ . The residual noise at low temperatures is somewhat higher than the intrinsic SQUID noise due to a slight mistuning of the electronics.

is  $\sim 6 \times 10^{-7} \Phi_0 / \sqrt{\text{Hz}}$ , a factor of 5 smaller than generated by the Au absorber and well below the noise produced by the SQUID.

A 1 mm thick sheet of copper, used for thermal contact, has a resistivity estimated to be  $2 \times 10^{-7} \Omega \text{ cm}$ . It is approximately 0.5 mm from and parallel to the plane of the pick up loop. The flux noise at 50 mK is, then,  $\sqrt{\mathcal{L}_\phi} \simeq 8 \times 10^{-7} \Phi_0 / \sqrt{\text{Hz}}$ . Although this noise source is not of importance in the present measurements, its magnitude does indicate that care is required in the use of metallic construction materials in the vicinity of the magnetometer.

### 4.3. Properties of Au:Er

The measured response of the calorimeter upon the absorption of an x-ray can be used to determine properties of the Au:Er system. Of particular interest to these measurements are the RKKY interaction and the origin of the initial fast decay of the signal pulse illustrated in Fig. 5. We discuss the RKKY interaction first.

#### 4.3.1. RKKY Interaction

The temperature dependence of the magnetization of a 300 ppm Au:Er sample depleted in the isotope with nuclear spin is shown at four different magnetic fields in Fig. 11. The data were taken with the large

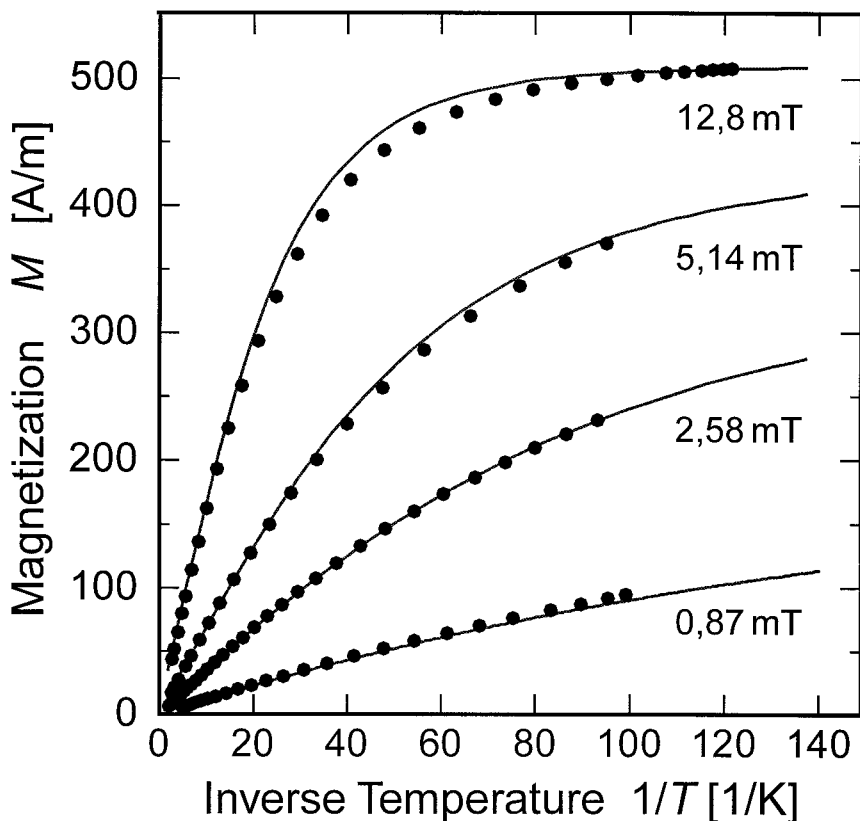


Fig. 11. The dependence of the magnetization upon inverse temperature of a 300 ppm sample at four different fields. The points are data while the lines are the result of the mean field calculation with  $\alpha = 5$ . The data was taken with the large calorimeter.

magnetometer, transformer coupled to the SQUID. The curves associated with the data points are theoretical results based on the mean field calculations with two adjustable parameters, the coupling factor and the RKKY interaction parameter  $\alpha$ . The data is best fit with  $\alpha = 5$ .

The dependence of the signal size on magnetic field and temperature can also be used to determine the strength of the RKKY interaction. The signal size,  $(\delta\phi_1 + \delta\phi_2)$  of Fig. 5, resulting from the absorption of a 122 keV x-ray is plotted in Fig. 12 as a function of magnetic field at several different temperatures. These data were obtained with the 300 ppm sample in the large magnetometer. The points are the experimental data, and the curves are theoretical fits to the data with just two parameters, the coupling factor

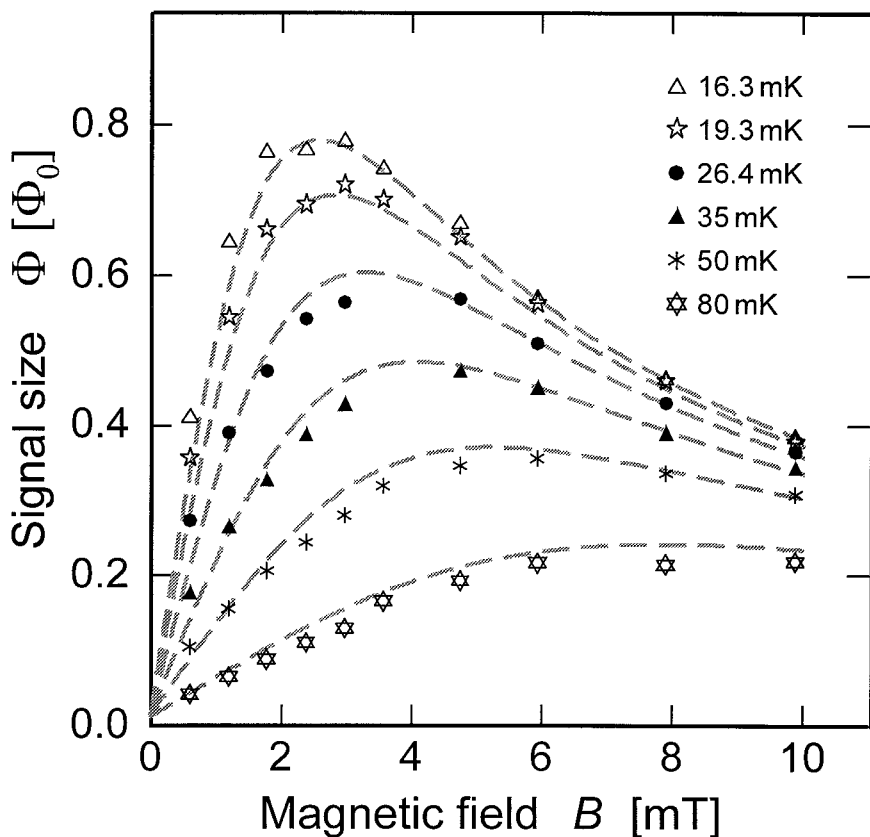


Fig. 12. Pulse height,  $\delta\phi_1 + \delta\phi_2$ , resulting from the absorption of 122 keV x-rays from  $^{57}\text{Co}$  versus magnetic field at several temperatures. The pulse height is the flux change in the SQUID in units of  $\Phi_0$ . The points were data taken with the large calorimeter while the lines are the result of the mean field calculation with  $\alpha = 5$ .

and the exchange interaction parameter,  $\alpha$ . The theoretical curves in Fig. 12 are the results of the mean field calculation with  $\alpha=5$ . Theoretical fits to the data are noticeably poorer with  $\alpha$  chosen 20% higher or lower, but a more careful analysis of the best choice of  $\alpha$  is not warranted given the approximations in the theory. The heat capacity (Er spins plus conduction electrons) calculated using the measured pulse height from Fig. 12 and  $\partial M/\partial T$  obtained theoretically is plotted in Fig. 13. Again, the curves are theoretical (mean field) fits to the data with  $\alpha=5$ .

While the fit of the mean field calculations to the data for the magnetization, signal amplitude and heat capacity appears good, there are observable systematic deviations between theory and experiment as seen,

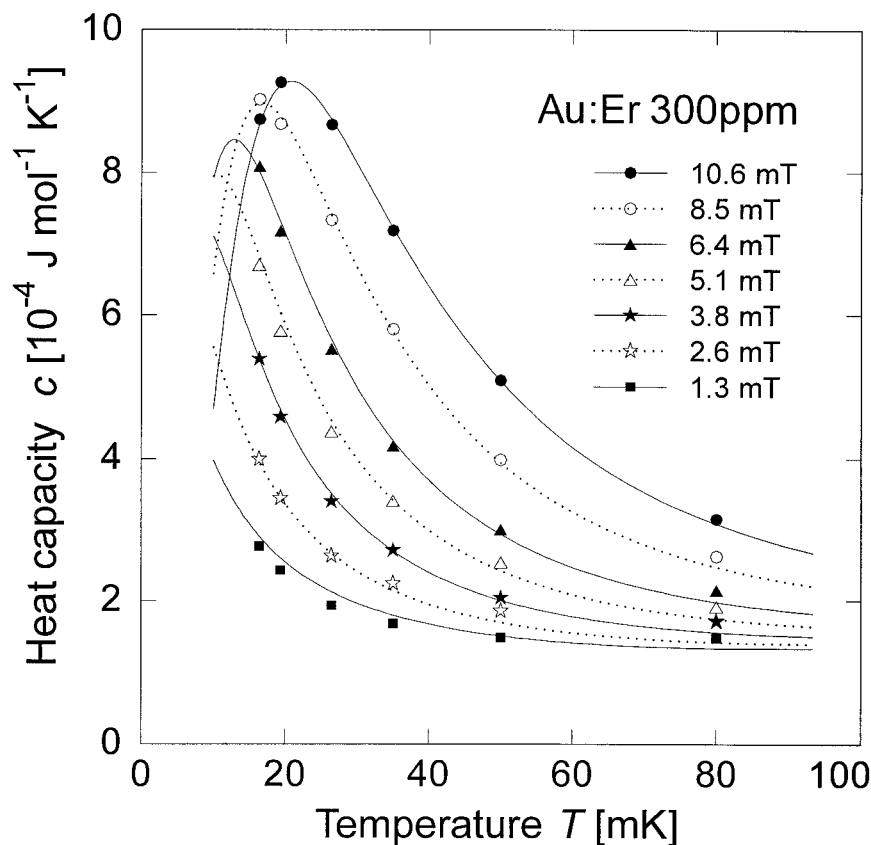


Fig. 13. The heat capacity of 300 ppm Er in Au as a function of temperature at several different fields. The points are computed using the data shown in Fig. 12. The lines are the result of the mean field calculation with  $\alpha=5$ .

for example, in the plot in Fig. 11 at 12.8 mT. Also, if the results of diagonalizing the Hamiltonian for a random distribution of spins<sup>10</sup> are used to fit the data, the value of the exchange parameter obtained is  $\alpha = 7$ . The difference in the values of  $\alpha$  found by the two methods is indicative of the limitations of the calculations. Furthermore, the calculations of the RKKY interaction are based upon a free electron gas with no consideration of real metal effects,<sup>31</sup> which are likely to be important at the level of agreement with experiment that is discussed here. Notwithstanding these caveats, the agreement is sufficient to demonstrate the degree to which the characteristics of magnetic calorimeters can be predicted.

The value of  $\alpha = 5$  required to fit the present data is somewhat larger than we reported earlier.<sup>8</sup> The reason for this difference is related to the use of unenriched Er in the earlier measurements. Although we took into account the heat capacity associated with the hyperfine interaction of 23 % abundant <sup>167</sup>Er, the calculation of the exchange interaction between localized moments did not include the influence of the hyperfine interaction on the characterization of the state of a <sup>167</sup>Er ion. At low temperature the ions with nuclear spin are in one of the states in the lowest  $F$  multiplet characterized by a specific  $m_F$ . The projection of the electronic spin onto such a state is reduced, and the exchange interaction is therefore correspondingly smaller. The omission of the hyperfine interaction in the calculation of the exchange interaction in the earlier measurements caused us to underestimate  $\alpha$  by about 40 %. On correcting for this oversight, the earlier measurements also indicate  $\alpha = 5$ .

#### 4.3.2. Additional Heat Capacity

Given what is known about the spin relaxation of Er in Au,<sup>11, 12</sup> the Zeeman/exchange system should achieve equilibrium with the conduction electrons faster than the SQUID can respond. The initial fast decay, characterized by the time constant  $\tau_1$ , must be the result of energy flowing out of the Zeeman system into another subsystem. As used above in the analysis of the RKKY interaction, the heat capacity of the spin system is proportional to  $(\delta\phi_1 + \delta\phi_2)^{-1}$  of Fig. 5. The field dependence of heat capacity of the additional subsystem, proportional to  $(\delta\phi_1)^{-1}$ , is illustrated in Fig. 14 at several temperatures.

One could make a different interpretation of the data, namely, that the time constant  $\tau_1$  is related with a part of the exchange system, such as clusters of spins that are ordering locally. These clusters would then come into thermal equilibrium on the time scale of  $\tau_1$  with the principal part of the Zeeman/exchange system. Such a picture appears untenable for several reasons.

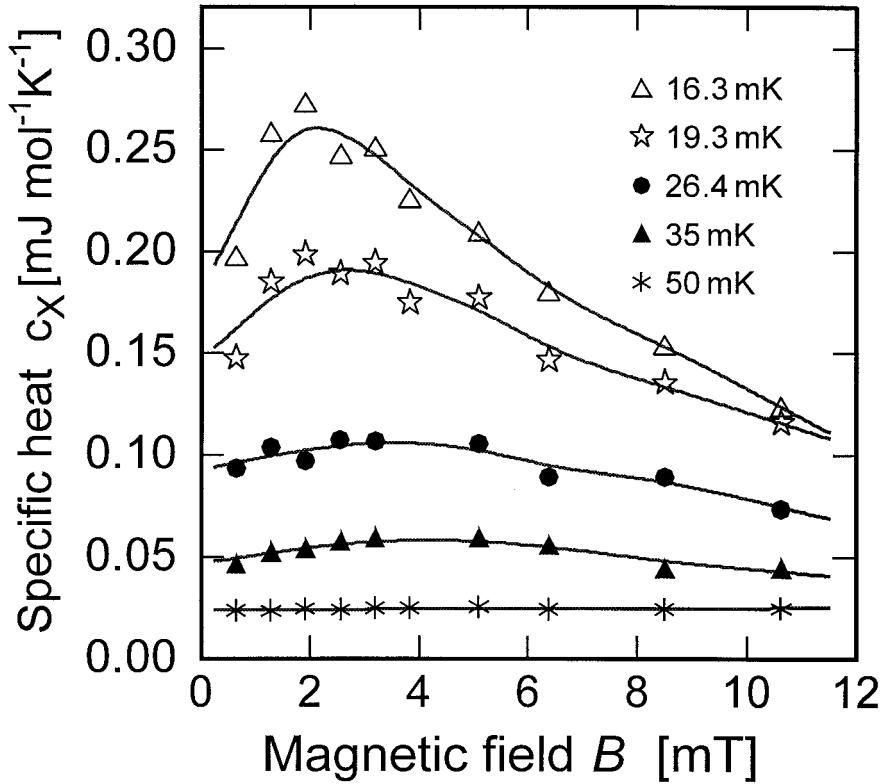


Fig. 14. The measured additional heat capacity associated with the flux change  $\delta\phi_1$  plotted as a function of temperature at several magnetic fields. The data was taken with the large calorimeter. The lines through the data points are guides to the eye.

(1) The spin-glass freezing temperature for 300 ppm Er in Au is known<sup>8</sup> to be  $\sim 1$  mK, well below the temperature of the present measurements. Substantial segregation of the Er ions would have to exist, for which there is no supporting evidence. Given the size of the additional heat capacity, these slowly relaxing clusters would have to contain a significant fraction of the total number of spins.

(2) If local spin ordering were the cause, then  $\tau_1$  should be strongly temperature dependent, contrary to observation, see Fig. 6a.

(3) In such a model the pulse amplitude,  $\delta\phi_2$ , would be the quantity that is inversely proportional to the heat capacity of the combined Zeeman-exchange system. The quantitative agreement between the measured values and the theoretical estimate of the spin heat capacity, illustrated in Fig. 13, would be destroyed.



The only active degrees of freedom, aside from the Er spins, capable of producing a heat capacity of the size measured below 50 mK are the spins of the gold nuclei.  $^{197}\text{Au}$  is 100 % naturally abundant. It has a nuclear spin of  $3/2$  with a small magnetic moment of 0.146 nuclear magnetons, but a relatively large quadrupole moment of  $+0.55b$ . Herrmannsdörfer *et al.*<sup>33</sup> have observed, using standard calorimetric techniques, a large heat capacity in a 600 ppm sample of Au:Er in the temperature range from 0.1 to 10 mK, see Fig. 15. The entropy as determined from those measurements is of a magnitude that it can only be associated with the nuclear spin degrees of freedom. It is our assumption that the heat capacity observed by Herrmannsdörfer *et al.*<sup>33</sup> and the additional heat capacity observed in the present measurements have the same origin.

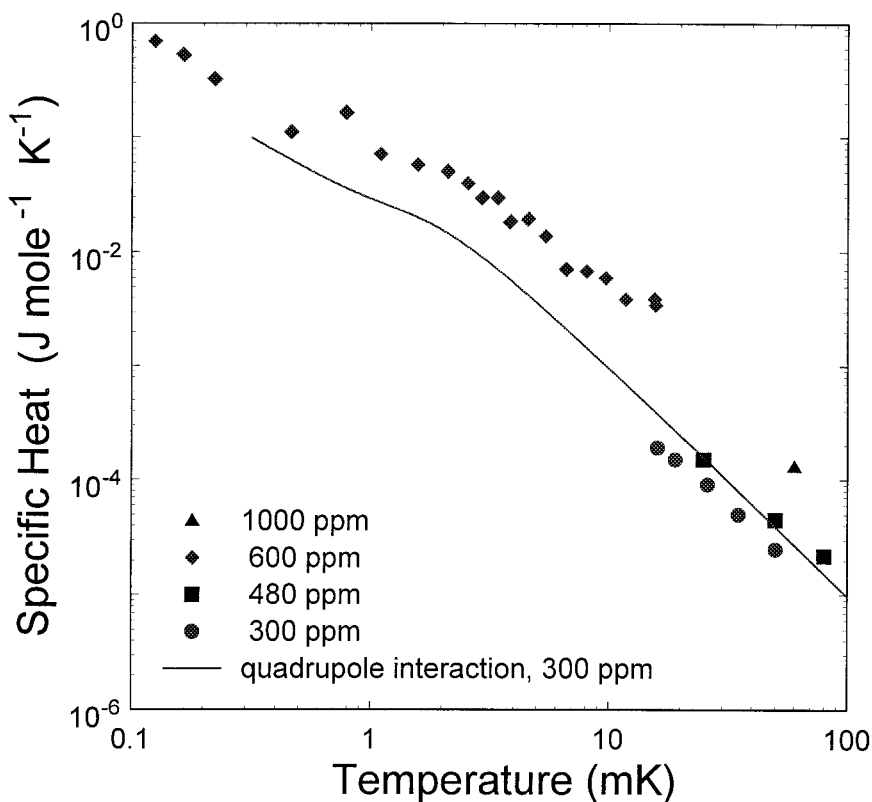


Fig. 15. The heat capacity of Au:Er 600 ppm measured by Herrmannsdörfer *et al.* to 0.1 mK shown in relation to the results of the current measurements on samples having concentrations of 300, 480 and 1000 ppm Er. The solid line is an estimation of the quadrupole heat capacity of the Au nuclei with 300 ppm Er, see text.

In Fig. 15 we have plotted the additional heat capacity determined from the present measurements as well as the results of Herrmannsdörfer *et al.*<sup>33</sup> The data suggests that the additional heat capacity depends upon Er concentration, but the evidence is hardly conclusive.

An Er ion in the gold lattice can interact with Au nuclei in its vicinity in two distinct ways. The magnetic moment of the Er ion couples to the nuclear moments of the Au via dipolar and indirect exchange interactions. Also, the presence of the Er ion distorts the lattice and, because of its different charge distribution, produces an electric field gradient at the site of the surrounding nuclei.

Consider the magnetic interaction first. The dipolar field of an Er ion at a nearest neighbor Au nucleus is the order of 0.1 T. Since the magnetic moment of Au is only  $0.15 \mu_N$ , the dipole interaction is much too small to contribute to the heat capacity at the temperature of the measurements. A magnetic field the order of 30 T at a nearest neighbor Au nucleus is needed to fit the data. The RKKY-type indirect exchange interaction, mediated by the conduction electrons, couples the effective spin  $\mathbf{S}$  of the Er ion to the nuclear spin  $\mathbf{I}$  of the Au and is of the form given by Eq. (5)

$$H_{\text{SI}} = \alpha_{\text{SI}} \frac{\mu_0}{4\pi} \frac{g\mu_B g_I \mu_N}{r^3} F(2k_F r) \mathbf{S}_i \cdot \mathbf{I}_j, \quad (34)$$

where  $g\mu_B \mathbf{S}$  and  $g_I \mu_N \mathbf{I}$  are the electronic moment of the ground state of the Er ion and the nuclear moment of Au respectively. The magnitude of the coefficient  $\alpha_{\text{SI}}$  can be estimated from the known indirect interaction between a pair of Er ions

$$H_{\text{S}} = \alpha_{\text{S}} \frac{\mu_0}{4\pi} \frac{(g\mu_B)^2}{r^3} F(2k_F r) \mathbf{S}_i \cdot \mathbf{S}_j, \quad (35)$$

and between pairs of Au nuclei

$$H_{\text{I}} = \alpha_{\text{I}} \frac{\mu_0}{4\pi} \frac{(g_I \mu_N)^2}{r^3} F(2k_F r) \mathbf{I}_i \cdot \mathbf{I}_j. \quad (36)$$

The various coefficients are related by

$$\alpha_{\text{SI}} = \sqrt{\alpha_{\text{S}} \alpha_{\text{I}}}. \quad (37)$$

This relation results from the following:  $\alpha_{\text{S}}$  depends upon the square of the exchange interaction,  $J_{\text{sf}}$ , between 4f electrons of an Er ion and the conduction

electrons;  $\alpha_I$  depends upon the square of the Fermi contact interaction,  $J_{sI}$ , of the conduction electrons with an Au nucleus; and  $\alpha_{sI}$  depends on the product  $J_{sf} \cdot J_{sI}$ . We have measured  $\alpha_s$  to be  $\simeq 5$ . The parameter  $\alpha_I$  has not, to our knowledge, been measured for gold. However, for Cu it has the value  $\alpha_I \simeq 0.7$ .<sup>34, 37</sup> From the ratio of the Knight shifts of Au and Cu,  $K_{Au}/K_{Cu} \simeq 6$ , we can estimate  $\alpha_I$  for gold. The Knight shift is linearly dependent on  $J_{sI}$ , and hence  $\alpha_I \simeq 0.7 \times 6^2 \simeq 25$  for gold. This leads to  $\alpha_{sI} \simeq 12$ , so that the indirect exchange is roughly an order of magnitude larger than the dipolar coupling between an Er ion and an Au nucleus. Nonetheless, this exchange interaction is still an order of magnitude smaller than required to explain the additional heat capacity.

Magnetic interactions between Er ions and Au nuclei of the size required to account for the heat capacity data can be ruled out on experimental grounds as well. The random orientation of the moments of the Au nuclei can, via the exchange, broaden the linewidth of the electron spin resonance of the Er ions. Von Spalden and Baberschke<sup>11</sup> measured residual ESR linewidths of less than 2 G for Er in Au. This result is consistent with  $\alpha_{sI} = 12$ , but is inconsistent with the value of 300 for  $\alpha_{sI}$ , which would be necessary to account for the heat capacity. The same holds true for the residual linewidth measurements of Sjöstrand and Seidel.<sup>12</sup>

The magnitudes of the electric field gradients (EFG) in metallic gold in the vicinity of an Er ion are impossible to estimate quantitatively without detailed calculations. The EFG depends sensitively on the electronic band structure of the metal and the polarization of the outermost core states.<sup>38, 39</sup> Small variations in the occupation of orbitals with different magnetic quantum numbers can have a major effect, even the sign of which is not easily predicted. In the absence of any real theoretical guidance we can only offer a plausibility argument as to how large the quadrupole interaction of Au nuclei with a neighboring Er ion might be. For the quadrupole interaction to be the source of the additional heat capacity requires the energy splitting of the  $\pm 3/2$  and  $\pm 1/2$  states of the nearest neighbor Au nuclei to be approximately 70 MHz. A splitting of 70 MHz corresponds to a field gradient of  $10^{22}$  V/m<sup>2</sup> at an Au nucleus. This is a large field gradient, but perhaps not unreasonably so. Although we are unaware of the EFG having been measured for Au nuclei in the vicinity of an impurity atom, Mossbauer studies<sup>40</sup> using the 77 keV  $\gamma$ -ray of <sup>197</sup>Au have measured quadrupole splittings of 300 MHz for Au in compounds. In Cu metal, the field gradient at a nearest neighbor to an impurity has been determined for a number of impurities.<sup>41</sup> For a Pd impurity the EFG is  $1.2 \times 10^{21}$  V/m<sup>2</sup> at a nearest neighbor, and for a Pt atom it is  $1.8 \times 10^{21}$  V/m<sup>2</sup>. While these fields are 5 to 10 times smaller than we require, Au is a larger and more deformable atom than Cu. In the free atoms, the Sternheimer antishielding

factor is close to 10 times larger for Au than for Cu,<sup>42</sup> so that it is not out of the question that the field gradients in the metals can have a similar ratio.

Another possibility we have considered is that the heat capacity of the nuclear spins is independent of the Er concentration. The apparent concentration dependence in the data shown in Fig. 14 could then be related with the different numbers of nuclei that achieve thermal equilibrium with the Er system. The Korringa constant for Au nuclei is  $K = 4.6 \text{ Ks}^{35}$  so that at low temperatures the relaxation of the nuclei must be associated with the Er.

Tunneling states can be ruled out as the cause of the additional heat capacity. Measurements of the low frequency sound velocity<sup>36</sup> exhibit a weak logarithmic dependence below 50 mK, which is typical for disordered solids such as amorphous and polycrystalline metals. Such a logarithmic dependence indicates a very broad (nearly constant) density of states. The heat capacity of such a system is known to depend linearly on temperature and can therefore not account for the excess heat capacity found in our calorimetric experiments. Moreover, the absolute value of the contribution of the tunneling states to the heat capacity, very roughly estimated, is several orders of magnitude too low to explain the excess specific heat. This estimate has been made by comparison with results for other polycrystalline metals, e.g., copper, for which both sound velocity and heat capacity have been measured.

Several mechanisms have been discussed in the literature<sup>37</sup> that could potentially result in an additional heat capacity at low temperatures. These include the interaction of the nuclear quadrupole moment with electric field gradients produced by strains, and a cooperative Jahn–Teller-type distortion of the lattice resulting in a decrease in energy of the Au nucleus on moving from a site of cubic symmetry. The estimation of the EFG produced by strains is even more problematic than calculating the EFG from an impurity. While strains in Au from handling and shaping the sample are likely to introduce EFG's that are much smaller than those produced by a substitutional impurity, many more nuclei in the sample could be affected than just those in the immediate vicinity of an Er ion. Strains cannot be ruled out as contributing to the quadrupole splitting of Au nuclei. A crude estimation of the Jahn–Teller transition suggests that it should occur in Au below  $1 \mu\text{K}$  and is unlikely to make a contribution to the heat capacity in the mK range.

In the absence of any viable alternate explanation we conclude that the most likely cause of the additional heat capacity is the quadrupole splitting of the Au nuclear spins due to the electric field gradients introduced by the presence of the Er ions. We have plotted in Fig. 15 the quadrupole heat capacity of a 300 ppm Er concentration in Au assuming a

splitting of 70 MHz for nearest neighbor Au nuclei. The energy splitting of more distant Au nuclei is assumed to depend upon separation from the Er ion in a manner similar to that found in Cu.<sup>41</sup> The roughly  $T^{-2}$  temperature dependence of the additional heat capacity observed in our measurements, as shown in Fig. 15, is consistent with a quadrupole splitting small compared to  $k_B T$ . The reason for the apparent field dependence of the quadrupole heat capacity, evidenced in Fig. 14, is not understood. Two possible explanations which come to mind are that it is an experimental artifact of the method by which we make the separation of  $\phi_1$  and  $\phi_2$  or that a varying fraction of the Au nuclei becomes thermally decoupled from the Er spins as magnetic field is increased. We tend to favor the latter explanation. The fact that the time constant  $\tau_1$  is independent of temperature indicates that the relaxation process is not thermally driven. Rather, it appears that the Au nuclei are coupled via a cross-relaxation process to the Er system. The energy splittings of the nuclei are thought to be roughly 70 MHz for nearest neighbors and to decrease rapidly as the distance to an Er ion increases. Thus, the resonant coupling of the nuclei and the Er system is presumably via energy splittings associated with the reorientation of Er spins in which the total magnetic quantum number of the Er remains constant, the quantity  $g\mu_B B$  being  $\sim 100$  MHz at 10 G. Why the overlap of the energy distributions of the two systems varies as  $1/B$ , required to explain the field variation of the time constant plotted in Fig. 6, is not obvious.

## 5. SUMMARY AND CONCLUSIONS

A magnetic calorimeter consisting of a metal doped with a low concentration of paramagnetic ions can be a fast, efficient and high-resolution detector of x-rays. Since the thermodynamic properties of such a system are well known, it is possible to determine the parameters, such as concentration of paramagnetic ions and size of calorimeter, that optimize the performance of a detector. Calculations of calorimeter performance have been confirmed by experiments using Er doped Au. While other materials may prove to be better magnetic sensors, the properties of Er in Au, with its large  $g$ -value and low RKKY interaction, are sufficiently favorable to make it an interesting choice. Even if one were able to find a system where the exchange interaction were zero, the presence of dipolar interactions would limit the improvement in sensitivity compared with Au:Er to less than 2 since  $S \propto \alpha^{-1/3}$ . The presence of the additional heat capacity presumed to be associated with the quadrupole splitting of the Au nuclei, while not beneficial, is not a serious detriment to the performance of a calorimeter.

Although the present measurements have achieved a relatively high energy resolution, an order of magnitude improvement should be obtainable, as relatively high noise levels have limited the performance.

A magnetic calorimeter has a number of features that make it attractive as a high-resolution energy detector.

- As the detector is a metal, the thermalization time is short at low temperatures. Of course, detectors dependent upon the measurement of properties not in thermal equilibrium, such as athermal phonons or tunneling currents, may be faster.

- With a magnetic sensor one measures magnetization, a bulk thermodynamic property, not a transport property. The response of a calorimeter can be calculated analytically from the known thermodynamic properties, and the design of a sensor can be optimized for a particular application.

- While magnetic sensors appear competitive with alternate cryogenic technologies for use in calorimeters with small heat capacities, they are particularly suited for detectors where large heat capacities are required. The sensitivity, proportional to  $C_a^{-1/3}$ , depends relatively weakly on heat capacity. Experiments in which large heat capacities are needed include the efficient detection of hard x-rays and the search for neutrinoless double beta decay. This research has been motivated in part by the need for large area ( $200 \text{ cm}^2$ ), high sensitivity sensors of helium scintillation for a proposed detector of low energy solar neutrinos.<sup>43</sup>

- Standard industrial processes may be applicable to the fabrication of certain types of magnetic calorimeters for x-ray detection. Not only can the SQUID and superconducting circuitry be produced by vapor deposition, the magnetic sensor and x-ray absorber may be as well. The combination of being fast and having the ability to handle large heat capacities without substantial degradation in sensitivity means that the calorimeter can be coupled to a heat reservoir with a relatively large thermal conductance. Sophisticated thermal isolation techniques may not be required.

## ACKNOWLEDGMENTS

We are indebted to H. Braun for his advice and for the use of his facilities for sample preparation, to R. Weis for his support in the laboratory, and to S. R. Bandler and H. J. Maris for helpful discussions. This work was supported in part by DFG (contract En299/2), NASA (Grant NAG5-5133) and NSF (Grant INT-9513904). G. Seidel gratefully acknowledges the support of the Alexander von Humboldt Stiftung.

## REFERENCES

1. M. B. Ketchen, D. D. Awschalom, W. J. Gallagher, A. W. Kleinsasser, R. L. Sandstrom, J. R. Rosen, and B. Bumble, *IEEE Trans. Mag.* **25**, 1212 (1989).
2. S. R. Bandler, C. Enss, R. E. Lanou, H. J. Maris, T. More, F. S. Porter, and G. M. Seidel, *J. Low Temp. Phys.* **93**, 709 (1993).
3. T. C. P. Chui, D. R. Swanson, M. J. Adriaans, J. A. Nissen, and J. A. Lipa, *Phys. Rev. Lett.* **69** 3005 (1992).
4. E. Umlauf, M. Bühler, and T. Fausch in *Phonon Scattering in Condensed Matter VII*, edited by M. Meissner and R. O. Pohl, Springer-Verlag, Berlin (1993) p. 490; E. Umlauf and M. Bühler in *Low Temperature Detectors for Neutrinos and Dark Matter*, edited by N. E. Booth and G. L. Salmon, Editions Frontieres, Gif-sur-Yvette (1991) p. 237.
5. P. G. de Gennes, *Compt. Rend.* **247**, 1836 (1958).
6. K. Yosida, *Theory of Magnetism*, Springer, Berlin (1996).
7. A. Abragam and B. Bleaney, *Electron Paramagnetic Resonance of Transition Ions*, Clarendon Press, Oxford (1970).
8. A. Fleischmann, J. Schönefeld, J. Sollner, C. Enss, J. S. Adams, S. R. Bandler, Y. H. Kim, and G. M. Seidel, *J. Low Temp. Phys.* **118**, 7 (2000).
9. L. R. Walker and R. E. Walsted, *Phys. Rev. B* **22**, 3816 (1980); L. R. Walker and R. E. Walsted, *Phys. Rev. Lett.* **38**, 514 (1977).
10. J. Schönefeld, Ph.D. thesis, University of Heidelberg (2000).
11. Y. von Spalden and K. Baberschke, *J. Mag. Mag. Mat.* **23**, 183 (1981).
12. M. E. Sjöstrand and G. M. Seidel, *Phys. Rev. B* **11**, 3292 (1975).
13. D. Pines and P. Nozieres, *The Theory of Quantum Liquids*, Benjamin, New York (1966).
14. J. J. Quinn and R. A. Ferrell, *Phys. Rev.* **112**, 812 (1958).
15. G. Tas and H. J. Maris, *Phys. Rev. B* **49**, 15046 (1994).
16. M. I. Kaganov, I. M. Lifshitz, and L. V. Tanatarov, *Zh. Eksp. Teor. Fiz.* **31**, 232 (1956) [*Sov. Phys.* **4**, 173 (1957)].
17. P. B. Allen, *Phys. Rev. Lett.* **59**, 1460 (1987).
18. H. J. Maris, private communication.
19. C. D. Tesche and J. Clarke, *J. Low Temp. Phys.* **29**, 301 (1977).
20. T. Varpula and T. Poutanen, *J. Appl. Phys.* **55**, 4015 (1984), see also B. J. Roth, *J. Appl. Phys.* **83**, 635 (1998).
21. D. T. Gillespie, *J. Appl. Phys.* **83**, 3118 (1998).
22. J. T. Harding and J. E. Zimmerman, *Phys. Lett. A* **27**, 670 (1968).
23. W. R. Smythe, *Static and Dynamic Electricity*, McGraw-Hill, New York (1939).
24. Obtained from Heraeus GmbH, Germany.
25. Obtained from Oak Ridge National Laboratory.
26. Quantum Design, 11578 Sorrento Valley Road, San Diego, CA 92121.
27. A. Fleischmann, C. Enss, J. Schönefeld, J. Sollner, K. Horst, J. S. Adams, Y. H. Kim, S. R. Bandler, and G. M. Seidel, *Nucl. Instrum. Methods A* **444**, 100 (2000).
28. J. Schönefeld, C. Enss, A. Fleischmann, J. Sollner, K. Horst, J. S. Adams, Y. H. Kim, S. R. Bandler, and G. M. Seidel, *Nucl. Instrum. Methods A* **444**, 211 (2000).
29. G. Hölzer, M. Fritsch, M. Deutsch, J. Härtwig, and E. Förster, *Phys. Rev. A* **56**, 4554 (1997).
30. An error was made in Ref. 28 in the ratio of the intensities of the  $K_{\alpha 1}$  and  $K_{\alpha 2}$  components. This led to a determination of the instrumental linewidth that was slightly too large.
31. P. A. Lingard, X. W. Wang, and B. N. Harmon, *J. Mag. Magn. Mater.* **54-57**, 1052 (1986); D. J. Miller and S. J. Frisken, *J. Appl. Phys.* **64**, 5630 (1988).
32. S. Aarjäs and G. R. Dunmyre, *J. Less-Common Metals* **10**, 220 (1966), see also L. R. Edwards and S. Levgold, *J. Appl. Phys.* **39** 3250 (1968).
33. T. Herrmannsdörfer, R. König, and C. Enss, *Physica B* **284-288**, 1698 (2000).
34. E. R. Andrew, J. L. Carolan, and P. J. Randall, *Phys. Lett. A* **37**, 125 (1971).
35. F. Pobell, *Matter and Methods at Low Temperatures*, Springer, Berlin (1996).
36. K. Horst, Diploma thesis, University of Heidelberg (1999).

- 37. K. Siemensmeyer and M. Steiner, *Z. Phys. B, Cond. Mat.* **89**, 305 (1992).
- 38. B. Drittler, M. Weinert, R. Zeller, and P. H. Dederichs, *Phys. Rev. B* **42**, 9336 (1990).
- 39. J. Ehmann and M. Fähnle, *Phys. Rev. B* **55**, 7478 (1997); A. Seeger, J. Ehmann, and M. Fähnle, *Z. Naturforsch. A* **51**, 489 (1996).
- 40. J. A. Sawicki, J. E. Dutrizac, J. Friedl, F. E. Wagner, and T. T. Chen, *Nucl. Instrum. Methods B* **76**, 378 (1993).
- 41. M. Minier and C. Minier, *Phys. Rev. B* **22**, 21 (1980); K. Konzelmann, G. Majer, and A. Seeger, *Z. Naturforsch. A* **51**, 506 (1996).
- 42. R. M. Sternheimer, *Z. Naturforsch. A* **41**, 24 (1986).
- 43. J. S. Adams, A. Fleischmann, Y. H. Huang, Y. H. Kim, R. E. Lanou, H. J. Maris, and G. M. Seidel, *Nucl. Instrum. Methods A* **444**, 51 (2000).